Monthly Notices
of the
ROYAL ASTRONOMICAL SOCIETY

MNRAS **493,** 477–495 (2020)
Advance Access publication 2020 January 23

doi:10.1093/mnras/staa186

Extreme variability in an active galactic nucleus: Gaia16aax

G. Cannizzaro [1,2★] M. Fraser [3] P. G. Jonker,[1,2] J. E. Pringle,[4] S. Mattila,[5] P. C. Hewett [4] T. Wevers,[4] E. Kankare,[5] Z. Kostrzewa-Rutkowska,[1,2,6] Ł. Wyrzykowski,[7] F. Onori [8] J. Harmanen,[5] K. E. S. Ford,[9,10,11] B. McKernan [9,10,11] and C. J. Nixon[12]

[1]*SRON, Netherlands Institute for Space Research, Sorbonnelaan, 2, NL-3584CA Utrecht, the Netherlands*
[2]*Department of Astrophysics/IMAPP, Radboud University, PO Box 9010, NL-6500 GL Nijmegen, the Netherlands*
[3]*School of Physics, O'Brien Centre for Science North, University College Dublin, Belfield, Dublin 4, Ireland*
[4]*Institute of Astronomy, University of Cambridge, Madingley Road, Cambridge CB3 0HA, UK*
[5]*Tuorla Observatory, Department of Physics and Astronomy, University of Turku, Väisäläntie 20, FI-21500 Piikkiö, Finland*
[6]*Leiden Observatory, Leiden University, PO Box 9513, NL-2300 RA Leiden, the Netherlands*
[7]*Warsaw University Astronomical Observatory, Al. Ujazdowskie 4, PL-00-478 Warszawa, Poland*
[8]*Istituto di Astrofisica e Planetologia Spaziali (INAF), Via Fosso del Cavaliere 100, Roma I-00133, Italy*
[9]*Department of Astrophysics, American Museum of Natural History, Central Park West at 79th Street, New York, NY 10024, USA*
[10]*Department of Science, Borough of Manhattan Community College, City University of New York, New York, NY 10007, USA*
[11]*Physics Program, The Graduate Center, City University of New York, New York, NY 10016, USA*
[12]*Department of Physics and Astronomy, University of Leicester, University Rd, Leicester LE1 7RH, UK*

Accepted 2020 January 10. Received 2020 January 9; in original form 2019 October 11

ABSTRACT

We present the results of a multiwavelength follow-up campaign for the luminous nuclear transient Gaia16aax, which was first identified in 2016 January. The transient is spatially consistent with the nucleus of an active galaxy at $z = 0.25$, hosting a black hole of mass $\sim 6 \times 10^8\,M_\odot$. The nucleus brightened by more than 1 mag in the *Gaia G* band over a timescale of less than 1 yr, before fading back to its pre-outburst state over the following 3 yr. The optical spectra of the source show broad Balmer lines similar to the ones present in a pre-outburst spectrum. During the outburst, the Hα and Hβ emission lines develop a secondary peak. We also report on the discovery of two transients with similar light-curve evolution and spectra: Gaia16aka and Gaia16ajq. We consider possible scenarios to explain the observed outbursts. We exclude that the transient event could be caused by a microlensing event, variable dust absorption or a tidal encounter between a neutron star and a stellar mass black hole in the accretion disc. We consider variability in the accretion flow in the inner part of the disc, or a tidal disruption event of a star $\geq 1\,M_\odot$ by a rapidly spinning supermassive black hole as the most plausible scenarios. We note that the similarity between the light curves of the three *Gaia* transients may be a function of the *Gaia* alerts selection criteria.

Key words: galaxies: active – quasars: supermassive black holes – galaxies: nuclei – accretion, accretion discs – transients: tidal disruption events – quasars: individual: Gaia16aax.

1 INTRODUCTION

Lying at the centre of galaxies, supermassive black holes (SMBHs) have an enormous impact on the region surrounding them. Once circumnuclear matter is close enough to the SMBH to fall into the gravitational potential, the black hole will start accreting this matter through the formation of an accretion disc if the material has angular momentum. These active galactic nuclei (AGNs) typically emit over the whole electromagnetic spectrum. Broad (1000–20 000 km s^{-1}) and/or narrow (300–1000 km s^{-1}) highly ionized emission lines are typically present in the optical spectra of AGNs. These lines come from clouds of matter in different regions and at different distances from the central black hole: the broad-line region (BLR) and the more distant narrow-line region (NLR). The presence or absence of broad and/or narrow lines leads to the classification of AGNs in 'types': Type 1 when both kinds of lines are present, and Type 2 when only narrow lines are present. Intermediate types, depending on the presence of single Balmer lines, exist, e.g. type 1.9 characterized by the presence of a broad Hα emission line but

★ E-mail: g.cannizzaro@sron.nl

with an absent broad H β (Osterbrock 1981). The unified model explains this dichotomy in terms of our viewing angle to the AGN, where a parsec-scale dusty torus may partially or totally obscure our view of the central engine and the BLR (Antonucci 1993; Urry & Padovani 1995).

AGNs are intrinsically variable objects, with stochastic variations in brightness of the order of 20 per cent over a time-scale of months to years and larger variations happening on longer time-scales (MacLeod et al. 2010, 2012). In recent years, more extreme examples of quasar[1] variability have been discovered, e.g. Graham et al. (2017) and Rumbaugh et al. (2018) found large samples of objects that showed variability of more than 1 mag over a time-scale of several years in an archival search in the Catalina Real-Time Transient Survey, Sloan Digital Sky Survey (SDSS), and Dark Energy Survey. Lawrence et al. (2016) investigated the nature of a sample of large-amplitude nuclear transients discovered during the Pan-STARSS 3π survey. The majority of these objects are classified as hypervariable AGNs. In some cases, AGNs will show slow and significant optical variability of more than 1 mag over several years, accompanied by spectral variability (e.g. Matt, Guainazzi & Maiolino 2003; LaMassa et al. 2015; MacLeod et al. 2016). These so-called 'changing-look AGNs' have been observed transitioning between different AGN types, with the (dis)appearance of broad emission lines (typically the Balmer series). While various physical mechanisms have been proposed to explain this extreme variability, such as variable obscuration across the line of sight, microlensing, or accretion disc instabilities, no single explanation has been found. Merloni et al. (2015) propose as an explanation the occurrence of a Tidal Disruption Event (TDE) in the nucleus of the galaxy. A TDE happens when a star passes so close to an SMBH that the tidal forces of the SMBH are stronger than the star's self-gravity. This leads to the (partial) disruption of the star (Hills 1975; Rees 1988; Evans & Kochanek 1989). The disruption of the star and the subsequent accretion of roughly half of the stellar material (the other half will be expelled on unbound orbits) give rise to a short and luminous flare that typically peaks in the UV or soft X-rays. The bolometric light-curve decay of the transient event is expected to follow the fallback rate of the material with a power-law decline $\propto t^{-5/3}$ on a time-scale of some months up to 1 yr (Evans & Kochanek 1989; Cannizzo, Lee & Goodman 1990; Lodato, King & Pringle 2009). TDEs have been invoked as a possible explanation also for numerous objects in the large samples described in Graham et al. (2017), Lawrence et al. (2016), and Rumbaugh et al. (2018).

Here, we report the follow-up observations of Gaia16aax, a transient event happening at the centre of a galaxy hosting a known QSO (SDSS J143418.47+491236.5, Abolfathi et al. 2018) at $z = 0.25$, discovered by the *Gaia* Science Alerts project (GSA; Hodgkin et al. 2013). The transient was given the designation AT2016dbt[2] in the Transient Name Server (TNS). The centre of the galaxy brightened by $\sim$1 mag (in the optical) over the course of 1 yr, before fading back to its pre-outburst state over more than 2 yr. Variability of similar amplitude is detected in X-rays. Together with the photometric variability, the object undergoes a dramatic change also in its spectroscopic characteristics. The broad Balmer lines (H α and H β), already present in the pre-outburst spectrum, during the outburst show a significantly different morphology, with two peaks of different intensities and separated by $\sim$100 Å. The initial classification spectrum showed a strong blue continuum with broad, double-peaked Balmer lines. After the initial classification as an AGN outburst, we started a multiwavelength follow-up campaign with optical and NIR photometry, optical spectroscopy, and X-ray observations.

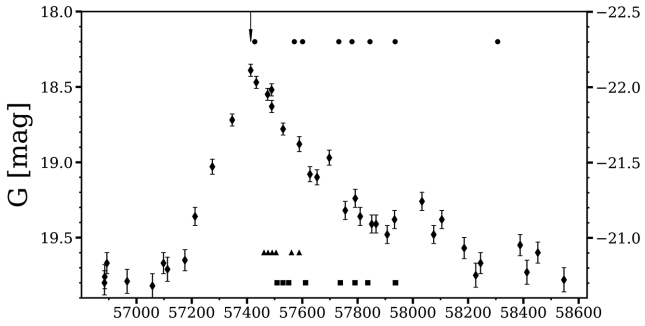

Figure 1. Light curve from the *Gaia* satellite for Gaia16aax. The arrow indicates the date the transient was alerted on. Magnitudes are in the *Gaia* *G* broad-band filter (Jordi et al. 2010). The black circles at the top indicate the epochs at which an optical spectrum was taken. The black triangles and squares at the bottom show the epochs at which optical and NIR images were taken, respectively. The two *y*-axes are apparent (left axis) and absolute (right axis) magnitudes.

In Section 2 we describe both the available, pre-outburst data and our own follow-up data, in Section 3 we describe our analysis of the photometric data, the spectral energy distribution (SED), and the fit to the emission lines, and finally in Section 4 we discuss our results in the broader framework of extreme AGN variability and we discuss some possible scenarios to explain the outburst.

Throughout the paper, we assume a cosmology with $H_0 = 67.7$ km s^{-1} Mpc^{-1}, $\Omega_M = 0.309$, and $\Omega_\Lambda = 0.691$, consistent with Planck Collaboration XIII (2016).

2 OBSERVATIONS

2.1 *Gaia* data and discovery

Gaia16aax was first alerted on by the *Gaia* Photometric Science Alerts programme[3] on 2016 January 26. The transient is $\sim$0.02 arcsec from the position of the host galaxy in the *Gaia* Data Release 2 (DR2; Gaia Collaboration 2018) and $\sim$0.1 arcsec from the position of the host galaxy in the SDSS (Abolfathi et al. 2018). As shown in Kostrzewa-Rutkowska et al. (2018), where nuclear transients detected by *Gaia* were matched astrometrically with SDSS sources, the astrometry provided by the *Gaia* Photometric Science Alerts system is accurate to $\sim$0.1 arcsec. We hence regard Gaia16aax as consistent with having no offset from the host nucleus. The *Gaia* light curve is shown in Fig. 1: It shows a steady, smooth rise up to its maximum in less than 1 yr and a slower decay on a time-scale of more than 2 yr to its pre-outburst, quiescent level. The apparent magnitude at peak in the *Gaia* broad *G* filter (which corresponds to white light; see Jordi et al. 2010) is $G = 18.39$, which corresponds to an absolute magnitude $M_G = -22.11$, given a source redshift $z \simeq 0.248$ and a luminosity distance $D_L = 1.26$ Gpc, assuming no extinction. The date of the alert issue corresponds with the date at which, according to the *Gaia* light curve, the flare reached its peak emission.

[1] We use the term Quasar or QSO to mean the most luminous fraction of the AGN population, with a bolometric luminosity of $L \gtrsim 10^{44}$ erg s^{-1}.
[2] https://wis-tns.weizmann.ac.il/object/2016dbt

[3] http://gsaweb.ast.cam.ac.uk/alerts/alert/Gaia16aax

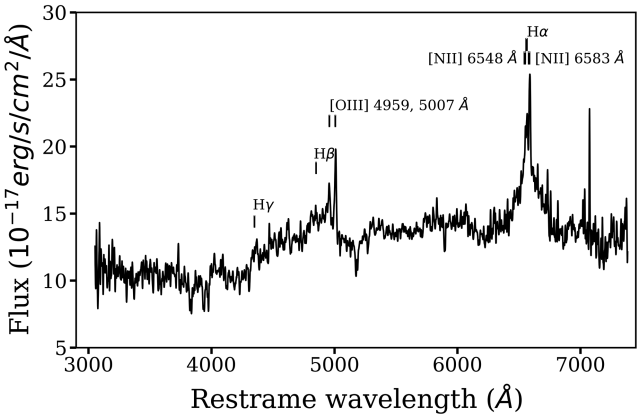

Figure 2. Archival spectrum from the SDSS legacy survey. The object shows broad Balmer emission lines and narrow forbidden oxygen and nitrogen lines.

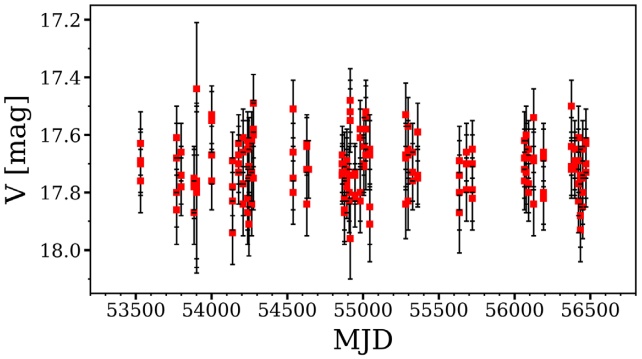

Figure 3. Historical light curve from the Catalina Sky Survey. In the period covered by the survey the source has not exhibited an outburst similar to Gaia16aax.

2.2 SDSS and Pan-STARRS

The source is present in SDSS Data Release 14 as SDSS J143418.47+491236.5. It was imaged on 2002 May 8[4] and morphologically classified as a galaxy with $r = 17.76 \pm 0.01$ mag. The source was then observed spectroscopically during the SDSS legacy survey on 2002 July 5 and classified as a broad-line quasar at redshift $z = 0.248\,53 \pm 0.000\,05$ Abolfathi et al. 2018. The SDSS spectrum is shown in Fig. 2. The point spread function-fitting (PSF) magnitudes are reported in Table A1. The object is also present in Pan-STARSS Data Release 2 as PSO J143418.490+491236.529 (Object ID 167052185770922854). The PSF magnitudes for the filters (*g, r, i, z*) are similar to, though not formally consistent with the ones reported in SDSS. The different values are likely due to the differences in the PSF modelling used in the two surveys.

2.3 Catalina Sky Survey

The source has been observed by the Catalina Sky Survey (CSS)[5] (Drake et al. 2009) over a period of 8 yr (from 2005 June to 2013 June, source ID CSS J143418.6+491236). As shown in Fig. 3, the object has not shown an enhanced emission state like Gaia16aax during the 8 yr of CSS monitoring.

2.4 2MASS

The source is present in the Two Micron All-Sky Survey (2MASS) as 2MASS J14341848+4912366. It has been observed once on 2000 May 7 in the three near-infrared bands *J*, *H*, and K_s, with magnitude values $J = 15.96 \pm 0.09$, $H = 15.47 \pm 0.14$, and $K_s = 14.64 \pm 0.10$.

2.5 (NEO)WISE

The source has been observed in the infrared band by both the *WISE* and the NEO-WISE (Near-Earth Objects Wide-field Infrared Survey Explorer; Mainzer et al. 2011) phases of the *WISE* satellite between 2014 January and 2017 June. This period has overlap with both the *Gaia* data (see Section 2.1) and our own follow-up data. The *WISE* satellite provides observations in four filters *W1*, *W2*, *W3*, and *W4* (3.4, 4.6, 11.6, and 22.1 μm, respectively), while the reactivation mission NEO-WISE only provides values for the *W1* and *W2* filters, in which it takes 10–20 single exposures for each epoch of observation. We selected only data points with photometric flags A or B [for which the minimum flux signal-to-noise ratio (SNR) is above 10 and 3, respectively]. The NEO-WISE magnitudes in the *W1* and *W2* bands in the quiescent phase (before MJD 57200) are compatible with the ones measured during the original *WISE* mission (Wright et al. 2010): $W1 = 13.783 \pm 0.025$ and $W2 = 13.17 \pm 0.02$ observed on 2010 July 21. The *WISE* magnitudes in the other two filters (not available during the NEO-WISE phase of the mission) are $W3 = 10.93 \pm 0.08$ and $W4 = 8.72 \pm 0.32$.

2.6 UV and X-ray observations

The source was observed with all the instruments onboard the Neils Gehrels Swift Observatory (Gehrels et al. 2004, *Swift* from here on) on 2006 September 9 and 14. UV data were analysed with the *Swift* task UVOTSOURCE, using a 5 arcsec aperture to estimate the source brightness and a 50 arcsec aperture, centred on a nearby empty region of sky, to estimate the background levels. Combining the two epochs of observations, we derived that the source has UV magnitudes $UVW1 = 21.5 \pm 0.2$, $UVM2 = 21.87 \pm 0.15$, and $UVW2 = 21.7 \pm 0.1$ (in the AB magnitude system).

In X-rays, the source was observed for a total exposure time of 14.2 ks. The X-Ray Telescope (XRT) data were analysed using the online XRT product builder (Evans et al. 2009). The observed flux in the 0.3–10.0 keV range is $2.5 \pm 0.9 \times 10^{-13}$ erg cm^{-2} s^{-1}, obtained modelling the data with a power law with a photon index $\alpha \sim 1.4$. This, at the luminosity distance reported previously, corresponds to a luminosity $L_X = 3.7 \pm 0.9 \times 10^{42}$ erg s^{-1}.

We observed the source again with *Swift* on 2019 July 18. The UV and X-ray data were reduced and analysed in the same way as the archival data. We derived UV magnitudes $UVW1 = 19.45 \pm 0.22$, $UVM2 = 19.38 \pm 0.24$, and $UVW2 = 19.52 \pm 0.23$. The 0.3–10.0 keV X-ray luminosity is $L_X = (1.7 \pm 0.7) \times 10^{43}$ erg s^{-1}. The object is therefore still bright in the UV and X-rays, with respect to the archival values.

We observed Gaia16aax also with *XMM–Newton*, for which we were awarded a Director's Discretionary Time observation. The observation started on 2016 June 30. During the observations, the pn camera was operated in Full Window mode, providing a time resolution of 73.4 ms. Both the MOS detectors were operated in

[4]from here onwards all times are in UTC.

[5]The CSS survey is funded by the National Aeronautics and Space Administration under Grant No. NNG05GF22G issued through the Science Mission Directorate Near-Earth Objects Observations Programme.

Partial Window mode, where the Small Window option was used, implying that only the central 100 × 100 pixels of 1.1 arcsec each were read out. This yields a time resolution of 0.3 s. The source flux is too low to yield meaningful Reflection Grating Spectrometer data.

We run the default SAS v17 (20180620) tool XMMEXTRACTOR under the HEASOFT FTOOLS software version 6.24 to extract source light curves and spectra. After filtering for periods of high background, we are left with a total exposure for the pn and MOS1 and MOS2 of 46.1, 59.7, and 59.4 ksec, respectively. We use the SAS command EPATPLOT to assess if photon pile-up is important during our observation. We conclude that pile-up is not important, as expected given the overall number of photons detected and given that the light curve does not show large flares.

The pn source spectrum was extracted from a circular region with a radius of 30 arcsec centred on the known optical source position. Background photons were extracted from a source-free circle with a radius of 59.59 arcsec centered on Right Ascension 218.527 and Declination 49.2065. The MOS source spectra were extracted from circular regions with a radius of 30 arcsec centered on the known optical source position. The MOS background spectra are obtained from an annulus centered on the source position, with inner and outer radii of 330 and 660 arcsec, respectively. The extracted spectra are rebinned to yield a minimum of 30 counts per bin.

We fitted the spectra with a power law modified by Galactic foreground extinction. The reduced χ^2 of the fit is 1.24 for 250 degrees of freedom. The normalization for the pn and MOS power laws is within a few per cent of each other, and we tie the other parameters ($N_{\rm H}$ and the power-law index) to require them to be the same. The best-fitting power-law index is 1.85 ± 0.01, while the foreground extinction is 2×10^{20} cm^{-2}. The 0.3–10 keV absorbed and unabsorbed flux is $(1.4 \pm 0.1) \times 10^{-12}$ and $(1.5 \pm 0.1) \times 10^{-12}$ erg cm^{-2} s^{-1}, respectively, corresponding to a luminosity of $(2.8 \pm 0.1) \times 10^{44}$ erg s^{-1}.

Simultaneously to the X-ray observation, we obtained photometry in the UV filters *UVM2* and *UVW1* and optical filter Johnson *U* with the Optical Monitor onboard of *XMM–Newton*. The resulting magnitudes are $UVM2 = 17.93 \pm 0.14$, $UVW1 = 18.15 \pm 0.04$, and $U = 18.32 \pm 0.03$, in the AB magnitude system.

2.7 NOT spectroscopic observations

We started a follow-up campaign of Gaia16aax using the Alhambra Faint Object Spectrograph (ALFOSC) using grism #4 [3200–9600 Å, (R∼360) for a slit of 1.0 arcsec] at the Nordic Optical Telescope (NOT), in the framework of the NOT Unbiased Transient Survey.[6] For all observations, the slit was placed at parallactic angle. We obtained 7 epochs of optical spectroscopy between 2016 February 9 and 2017 July 1 (see Table 1). All observations were reduced using FOSCGUI,[7] which is a pipeline based on standard `iraf` data reduction procedures: flat-field and bias correction, cosmic ray cleaning, wavelength and flux calibration with arc lamps and standard stars and telluric line correction (Tody 1986). The pipeline also performs second-order contamination removal for the spectra following Stanishev (2007). The sequence of ALFOSC spectra is shown in Fig. 4.

[6] http://csp2.lco.cl/not/

[7] FOSCGUI is a graphic user interface aimed at extracting SN spectroscopy and photometry obtained with FOSC-like instruments. It was developed by E. Cappellaro. A package description can be found at http://sngroup.oapd.inaf.it/foscgui.html.

Table 1. ALFOSC/NOT spectroscopic observations.

MJD[a] (d)	UTC date	Exposure time (s)	Slit (arcsec)	Airmass
57428.27	2016 Feb 10	2400	1.0	1.07
57571.06	2016 Jul 2	1800	1.0	1.56
57600.97	2016 Jul 31	2700	1.0	1.49
57732.25	2016 Dec 10	1800	1.0	1.76
57780.26	2017 Jan 27	2400	1.0	1.11
57845.15	2017 Apr 2	2700	1.0	1.07
57935.94	2017 Jul 1	2000	1.3	1.10
58307.01	2018 Jul 8	2700	1.0	1.32

Note. [a]Modified Julian Day of observations.

On 2018 July 8, we took one last spectrum to verify that the object had returned to quiescence as suggested by its *Gaia* light curve (see Fig. 1). Indeed, this spectrum appears to be similar to the pre-outburst SDSS spectrum and dividing the two spectra results in an almost featureless spectrum but with a slight slope. The slope and the presence of residual Hα and [O III] lines can both be introduced due to the use of different spectrographs by SDSS (optical fibres) and NOT (long slit): an optical fibre will collect more light from the whole galaxy, while the slit is centred on the nuclear region, hence the SDSS spectrum will have an excess of light coming from the circumnuclear region (see Fig. 5).

2.8 Photometric observations

Besides our spectroscopic follow-up, we started a series of photometric observations to monitor the decay of the transient to complement the light curve from *Gaia*. These photometric observations were also performed in the framework of the NOT Unbiased Transient Survey using NOTCam (Nordic Optical Telescope near-infrared Camera and spectrograph) at the NOT for the NIR bands *J*, *H*, and K$_s$. In addition, we employed the Optical Wide Field camera (IO:O) at the Liverpool Telescope (LT) using the Sloan *ugriz* and Bessel *B* and *V* filters. After the source went back to its pre-outburst emission level, we obtained a final set of observations in all necessary filters to subtract the host-galaxy/pre-outburst contribution to the flux detected in outburst. The NOTCAM images were reduced using a modified version of the external NOTCAM IRAF package[8] (version 2.5) and their zero-points calibrated using the 2MASS (Skrutskie et al. 2006) catalogue. Optical images were reduced through the LT pipelines and their zero-points were calculated using stars in SDSS. For the calculation of the zero-points in Bessel *B* and *V*, we applied the filter transformation equations found in Jester et al. (2005).

For each epoch of observation, we performed differential photometry to measure the magnitude of the transient. For this, we subtracted a template image, taken when the object was back at its pre-outburst emission level, from our scientific images, using `hotpants`[9] (Becker 2015). This program uses the algorithm from Alard & Lupton (1998) for the subtraction of images taken under different seeing conditions: It applies a spatially varying kernel to one of the two images to match the PSF of the other one and then subtracts the template image to obtain a final image in which only the transient is visible, while all constant luminosity sources will have been subtracted.

[8] http://www.not.iac.es/instruments/notcam/guide/observe.html#reductions

[9] https://github.com/acbecker/hotpants

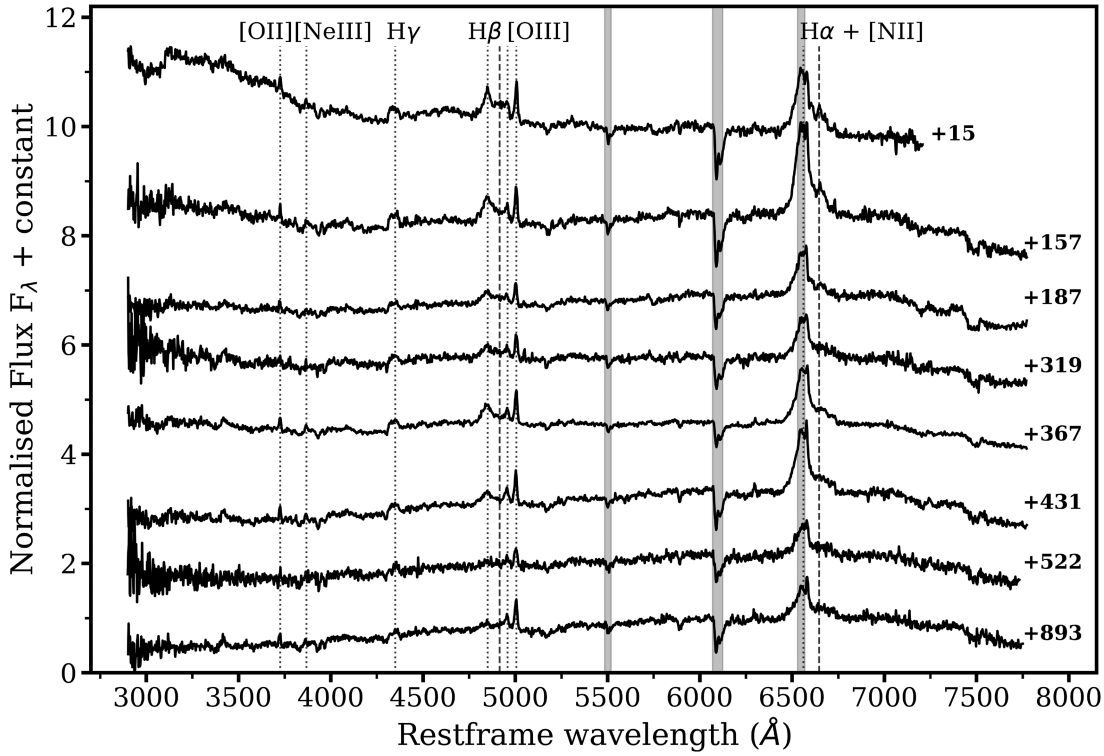

Figure 4. Eight optical spectra taken with ALFOSC at the NOT, shifted to the rest frame of the host galaxy. For each spectrum, we annotate to the right the number of days passed since the publishing of the *Gaia* Science Alert (2016 January 26; see Section 2.1). Note the large gap in time between the first and second spectroscopic observations. The dotted lines indicate the wavelengths of the main emission lines, and the dashed lines indicate the secondary components (red wings) of the H α and H β lines. The grey bands represent wavelengths affected by the telluric absorption, one of which affects the H α line region.

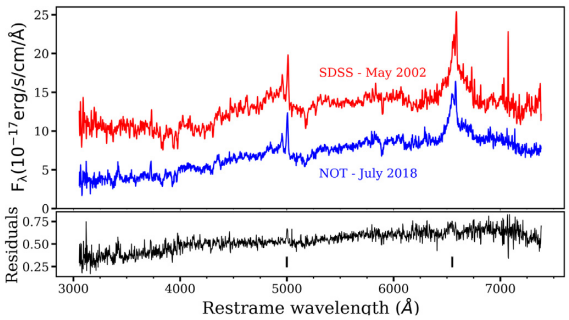

Figure 5. Comparison between the SDSS pre-outburst spectrum (in red) and the last spectrum of our follow-up (2018 July, in blue). The division of the two spectra results in a nearly featureless spectrum, shown in the bottom panel. In the residual spectrum, there is still a trace of the H α and [O III] emission lines (marked in the bottom panel).

On these subtracted images, we performed aperture photometry using the `iraf` task `apphot` with variable apertures depending on the seeing conditions. Uncertainties on the magnitudes are obtained by adding in quadrature the photometric error from the aperture photometry and the standard deviation due to the scatter in the sources used to calculate the zero-points. We did not apply band-pass corrections as our uncertainties are dominated by systematic errors due to the image-subtraction process.

2.9 Observations of other *Gaia* transients

In the first few months of 2016, other two objects with very similar characteristics to Gaia16aax were discovered by the *Gaia* Photometric Science Alerts pipeline: Gaia16ajq[10] (AT2016dvz on the TNS) and Gaia16aka[11] (AT2016dwk on the TNS).

Gaia16ajq was discovered on 2016 March 29, as an increase in brightness by ∼1 mag in the nucleus of an active galaxy at z∼0.28. The galaxy is present in SDSS and it is classified as a QSO/starburst galaxy. Gaia16aka was discovered on 2016 March 31 also as an increase in brightness of ∼1 mag of the nucleus of a galaxy at z∼0.31. This galaxy is present in SDSS but an archival spectrum is not available; therefore, we were unable to determine if the galaxy hosts an AGN.

In Fig. 6, the *Gaia* light curves of Gaia16ajq and Gaia16aka, together with the one of Gaia16aax, are plotted. The light curves have been aligned using the time of peak as point of reference and shifted vertically by 0.1 mag for comparison. All three objects show a similarly shaped rise to peak emission on the same time-scale of a few hundreds of days. The light-curve decay of the three objects is less similar than the rise time. All three objects show bumps in the decay part of the light curve, with Gaia16ajq showing two very prominent ones at ∼200 and ∼400 d after peak.

The three objects show similarities also in their spectra. For Gaia16ajq and Gaia16aka, we only have a classification spectrum, taken with the NOT a few days after discovery. Both spectra and the first spectrum of Gaia16aax, for comparison, are shown in Fig. 7. All the three objects show a blue bump – with Gaia16aka showing the most prominent one – broad Balmer lines and narrow forbidden lines typical of AGNs. In all three spectra, the continuum between

[10] https://gsaweb.ast.cam.ac.uk/alerts/alert/Gaia16ajq/
[11] https://gsaweb.ast.cam.ac.uk/alerts/alert/Gaia16aka/

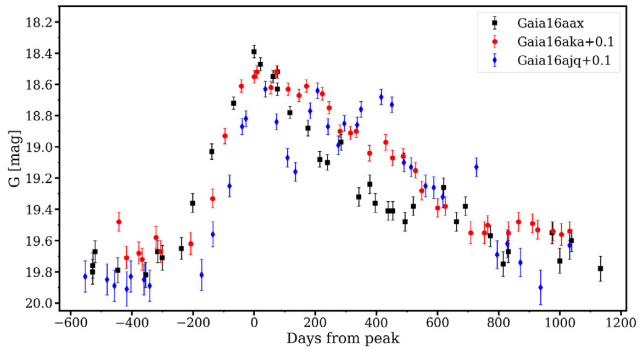

Figure 6. Light curves of the three similar sources found by the *Gaia* Alerts system: Gaia16aax (black squares), Gaia16ajq (blue diamonds), and Gaia16aka (red circles). For the sake of comparison, all three light curves have been shifted vertically and horizontally. The 0 on the *x*-axis is the date at which each object reaches its peak emission.

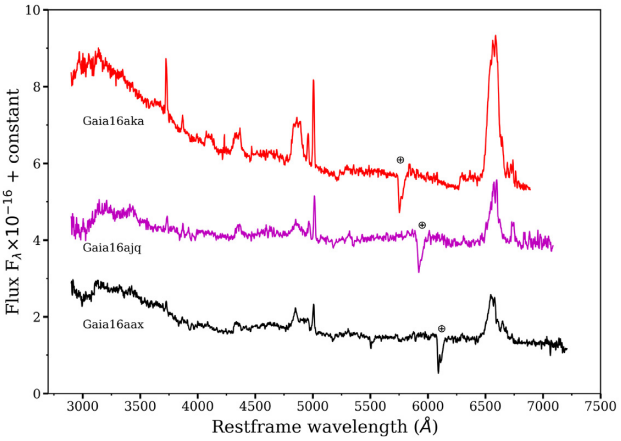

Figure 7. Spectra of the three similar Gaia objects: Gaia16aka (at the top, in red), Gaia16ajq (in the middle, in magenta), and Gaia16aax (at the bottom, in black). With ⊕ we indicate telluric absorption bands.

H γ and H β is high; this could be due to the presence of unresolved lines due to the Bowen fluorescence mechanism or to a forest of unresolved Fe lines.

While the H α and H β lines in Gaia16aax showed a very distinct double-peaked shape during the outburst, both Gaia16ajq and Gaia16aka do not show the same morphology in their spectra.

3 ANALYSIS AND RESULTS

3.1 Photometric and SED analysis

The *Gaia* light curve shown in Fig. 1 shows a decay from the peak of the emission to the pre-outburst level of emission over more than 2 yr. The light curve shows two bumps at around 57700 and 58000 MJD (around 300 and 600 d from peak, respectively). The decay rate is well fitted by an exponential decay $\sim t^{-0.161\pm0.004}$ (with $\chi^2_\nu = 0.97$). As shown in Fig. 8, where we compare the NEO-WISE light curve with the *Gaia* one, Gaia16aax reaches the peak of its MIR emission with a delay of ∼140 d with respect to the optical data. We assumed the epoch at which the NEO-WISE reaches its peak to be the one corresponding to the maximum observed value (MJD ∼57554). As the NEO-WISE light curve is not as well sampled as the *Gaia* one, the peak of the light curve could have happened at

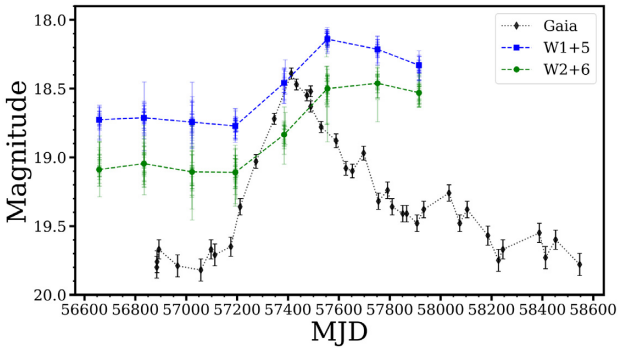

Figure 8. Light curve from the NEO-WISE mission, compared with the *Gaia* light curve. Plotted are the magnitudes in the two filters *W1* (blue) and *W2* (green), shifted along the *y*-axis to allow a comparison with the *Gaia* data. The solid blue squares (*W1*) and green circles (*W2*) are the mean values of the exposures taken for each epoch. The NEO-WISE light curve reaches its peak with a delay of ∼140 d with respect to the *Gaia* light curve.

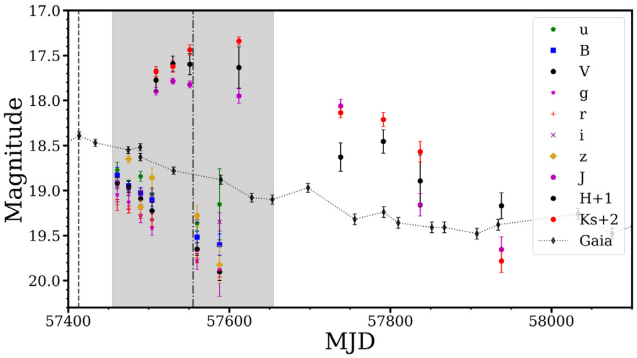

Figure 9. Light curve of the NOT and LT observations in the optical and NIR bands, compared with the *Gaia* light curve. The vertical dashed line at MJD 57413 corresponds to the date the alert was published while the vertical dashed line at MJD 57555 and the grey area indicate the time frame in which the NEO-WISE light curve reaches its peak. The magnitudes plotted are the ones resulting from the host-subtraction process.

a different epoch. None the less, since the light curve evolution is smooth, we expect our estimate to be good to 100 d, which is half of the interval between consecutive WISE observations. The delay between the *WISE* and *Gaia* light curve is of 140 ± 100 d. Assuming that the MIR emission comes from a dusty torus surrounding the BLR, this delay would imply a distance of this torus from the central engine of 0.12 ± 0.08 pc.

The light curve of NIR and optical bands is shown in Fig. 9, and the apparent magnitudes after the host subtraction are listed in Table A1. The light curve shows a smooth decay, consistent with the behaviour observed in the *Gaia* light curve. There is a bump in the *H* band around 57800 MJD; this is around 100 d after the bump in the *Gaia* light curve at 57700 MJD, a value that is consistent with the delay present in the NEO-WISE light curve. The colour evolution is shown in Fig. 10: all colours have been fitted both with a constant value and with a slope. The reduced χ^2 in all cases is well below 1, meaning that the uncertainties on the colour are too large to determine an evolutionary trend of the colours. We also performed a KS test to assess the goodness of fit and found that the colours $B-V$ and $r-i$ are better fitted with a slope than with a constant. Therefore, while the $g-r$ and $u-g$ remain constant over the period of observation, the colour $B-V$ decreases from

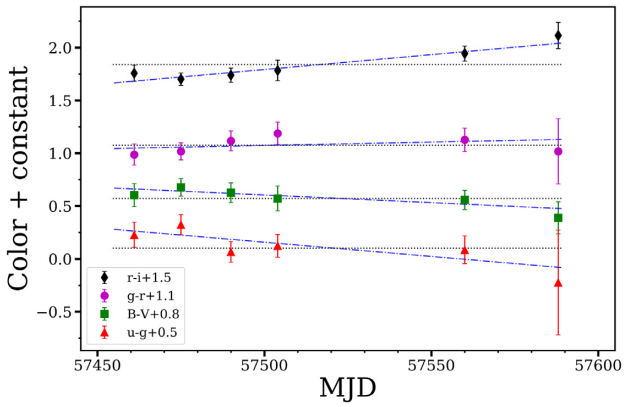

Figure 10. Colour evolution of $r-i$ (black diamonds), $g-r$ (magenta circles), $B-V$ (green squares), and $u-g$ (red triangles). For all the colours, both a fit with a constant line (black dotted lines) and a fit with a slope (blue dashed lines) are shown. The colours are calculated from the host-subtracted magnitudes.

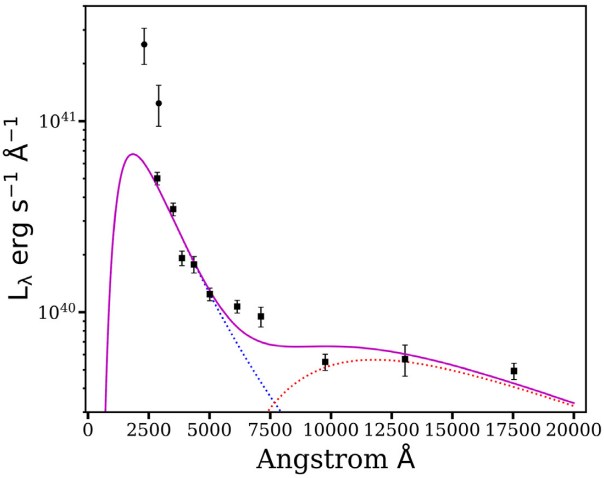

Figure 11. Fit of two blackbody curves to the luminosity density. The black squares are the values of the luminosity for each filter (optical – MJD 57505 and NIR – MJD 57509), the black circles are the two values of the monochromatic luminosity for the two UV filters *UVM2* and *UVW1* (MJD 57569, not considered for the fit), the solid magenta line represents the fit using two blackbody components, and these two components are represented by the blue and red dotted lines. On the x-axis there is the rest-frame wavelength.

-0.2 ± 0.1 to -0.4 ± 0.1 and $r-i$ increases from 0.3 ± 0.1 to 0.6 ± 0.1.

The host-subtracted and extinction-corrected magnitudes were used to model the SED and calculate the bolometric luminosity of the object using a `python` code adapted from the program `superbol` (Nicholl 2018). For all filters the extinction correction was done using the values in Schlafly & Finkbeiner (2011), who assume a reddening law with $R_v = 3.1$. Our NIR and optical data are not coincident in time; therefore, we focused on the epochs in which we had optical data, adding the NIR points to better constrain the fit where possible, and extrapolating or interpolating the NIR data to match the epochs of optical imaging. However, since our first NIR observations (MJD 57509.04) are almost coincident with our fourth epoch of optical data (MJD 57505.03), we decided to add NIR data only from MJD 57491.01 (the third epoch of optical imaging) onward, to avoid large extrapolation of the NIR data. The total bolometric luminosity is then calculated by connecting the points in the optical wavelengths with straight lines and integrating the area under the resulting curve, plus a blackbody extrapolation in the UV and NIR regions. For every epoch, we applied a K-correction to the data and then fit the fluxes derived from each band with two blackbodies. An example of the fit is shown in Fig. 11.

The absence of UV data-points hinders our ability to constrain the peak of the blackbody emission. Using the UV data from our single *XMM–Newton* observations, we can check our choice of using two blackbodies instead of one for the optical and NIR observations closest in time to the *XMM–Newton* observation: subtracting the pre-outburst UV flux measured by *Swift* from the values measured from the *XMM–Newton* observation for the *UVM2* and *UVW1* filters (central wavelength 2310 and 2910 Å, respectively), we obtain a luminosity density of $\sim 3.2 \times 10^{41}$ and $\sim 1.5 \times 10^{41}$ erg s^{-1} Å^{-1}, respectively. These values are higher than the peak of our fit, suggesting that by using two blackbodies we are not overestimating the emission from the object.

Modelling the SED with two blackbody curves does not yield a good fit (reduced $\chi^2 \sim 4$–5 for all epochs). On the one hand, our NIR and optical magnitudes are not coincident in time, thus introducing some systematic uncertainty in our SED. On the other hand, there is probably a non-thermal component that we are not considering in our fit. This is also hinted at by the high values of the UV and X-ray luminosities. The absence of UV data, though, hinders our ability to constrain the parameters of a power law that would probably describe the non-thermal component. On top of this, we see emission from more than one component: the optical and the (delayed) infrared emission (see Fig. 8). All in all, we assume that our fit using two blackbodies is a reasonable first-order description of SED and allows for an estimate of the bolometric luminosity.

The bolometric luminosity resulting from the blackbody fits is plotted in Fig. 12. The bolometric luminosity of the object decreases by a factor of 2 over $\sim$300 d and then remains constant within uncertainties at around $\sim 3 \times 10^{44}$ erg s^{-1}. The temperature and radius for both blackbodies remain constant during all the period of observation. The peak of the two blackbodies curves is at $\sim$1000 Å and $\sim$1 μm. The blackbody temperature of the second blackbody component (associated with the IR emission) is high, above 2000 K, indicating the presence of dust possibly above the evaporation temperature.

We calculated the bolometric correction to the absolute magnitude from *Gaia* with the values of the bolometric luminosity obtained from the photometric measurements. We then calculated the average of the correction over the epochs of observations and, under the assumption that this correction remains constant, used it to estimate the bolometric luminosity from the *Gaia* absolute magnitudes over the duration of the whole outburst. With this method, we were able to calculate the estimated total energy irradiated: $E_{\rm tot} = (3.3 \pm 0.9) \times 10^{52}$ erg. The uncertainty on this measure has been calculated by propagating the uncertainty on the bolometric luminosity from our photometric measurements. As the *Gaia* magnitudes are given without uncertainty, the error on the total energy radiated during the outburst derives only from the error on the bolometric luminosity we calculated.

The bolometric luminosity evolution as a function of time calculated from the *Gaia* magnitudes mimics the shape of the *Gaia* light curve by design; therefore, the decay trend of the bolometric luminosity is also well fitted by an exponential decay $\propto t^{-0.16 \pm 0.01}$.

We use the luminosity in the X-ray, calculated from the *XMM* observation, in the band 2–10 keV, $L_{2-10\,\rm keV} = (1.2 \pm 0.1) \times$

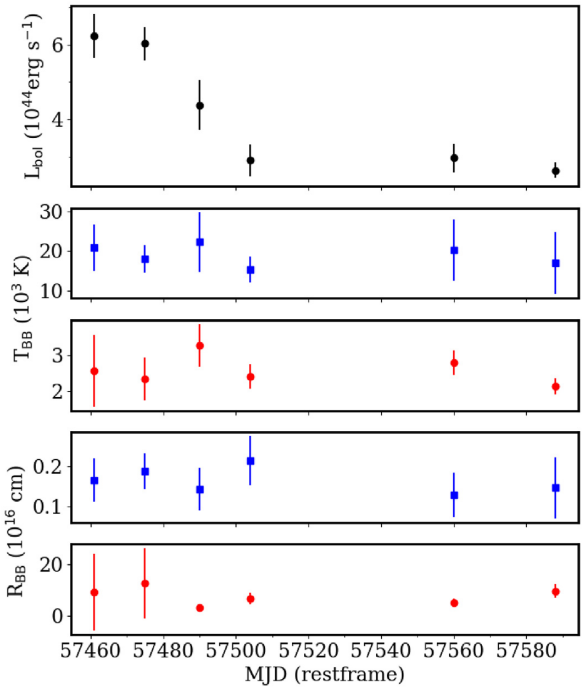

Figure 12. Results from the blackbody fits to the flux density at each epoch. In the top panel we plot the bolometric luminosity, in the second and third panels we plot the temperature for the two blackbodies, and in the fourth and last panels the radius for the two components (blue squares for the first blackbody and red circles for the second one, in all relevant panels. The first blackbody is the one that peaks at shorter wavelengths, the second one is the one that peaks at larger wavelengths; see Fig. 11). The large uncertainties on the blackbody parameters in the first two epochs (especially for the radius of the second blackbody component) are due to the absence of NIR data.

10^{44} erg s^{-1}, to have another estimate of the bolometric luminosity. To do this, we calculate the values of the bolometric correction (k_{bol}) using the methods described in Marconi et al. (2004) and Netzer (2019). We obtain $k_{bol} \simeq 34$, using the equation of Marconi et al. (2004) and $k_{bol} \simeq 29.6$ from Netzer (2019). The resulting luminosity values are $L = 4.2 \times 10^{45}$ and 3.6×10^{45} erg s^{-1}, respectively. The uncertainties in these values are dominated by the uncertainties in the evaluation of the bolometric correction, but they are not easy to calculate. The range in the extreme values of k_{bol} can be as large as an order of magnitude (Netzer 2019) and depends strongly on the constraints used to calculate k_{bol}. We note that the value of the bolometric luminosity estimated from the X-ray luminosity is higher than the one calculated from the SED fit. This is in agreement with the statement that our SED fit probably underestimates the bolometric luminosity, given the absence of UV and X-ray data points. If we, instead, compare the $L_{2-10\,keV}$ with the bolometric luminosity obtained from the SED fit, we would get a value of $k_{bol} \sim 2.5$. This value is much lower than what is reported in the literature (Marconi et al. 2004; Brightman et al. 2017; Netzer 2019). We therefore consider that the value of the total energy radiated over the outburst, obtained from the SED fit, is underestimated.

3.2 Spectroscopic analysis

We used the first spectrum (MJD 57428.27) to classify the transient event. This was done by cross-correlating our classification spectrum with a library of spectra using the `snid` code (Blondin & Tonry 2007), resulting in a good match with an AGN spectrum (Mattila et al. 2016). The redshift calculated from the transient spectrum is consistent with the one reported in SDSS.

In Fig. 4, we plot all the spectra of our follow-up campaign. Looking at the follow-up spectra by eye, the first optical spectrum shows a blue component, while during the decay of the outburst the spectra become redder. Broad Balmer lines (Hα, Hβ, Hγ) are present in all spectra, as well as the narrow [O III] and [N II] lines. These lines are present in the SDSS quiescent spectrum, but both their intensity and structure appear to be changed in the outburst spectra. This is likely due to the difference of spectral and spatial resolutions of the spectrographs employed by SDSS and NOT. The region of the Hβ broad emission line is complex with various broad components and narrow [O III] ($\lambda\lambda$4959 and 5007) emission lines. The Hα line is contaminated by the telluric absorption around 8250 Å; this hindered our ability to fit in detail the properties of the emission lines in this wavelength region. At the first epoch, there is a bump in the continuum between Hγ and Hβ. This is possibly due to a complex of unresolved lines such as that caused by the Bowen fluorescence mechanism (Bowen 1934, 1935) blended with He II at 4686 Å. Metal lines originating from the Bowen fluorescence have been recently reported to be present in TDEs (Blagorodnova et al. 2019; Leloudas et al. 2019; Onori et al. 2019). In the subsequent spectra, this blend is not present anymore.The absence of other strong lines typically associated with the Bowen fluorescence mechanism, such as N III $\lambda\lambda$4640, 4100 and [O III] λ3760, could hint that this is instead a forest of iron lines typically seen in an AGN. It is worth noting that this higher continuum is not present as distinctly as in the first spectrum at other epochs, hinting at a possible transient nature of the unresolved lines.

The spectra show a significant galaxy emission component and various galaxy absorption lines, most notably the Ca H&K lines (3969 and 3934 Å, respectively). To model the galaxy emission, we use the penalized Pixel-Fitting method `ppxf` (Cappellari & Emsellem 2004; Cappellari 2017). The method approximates the galaxy spectrum by convolving a series of N template spectra $T(x)$ with an initial guess of $f(v)$, the line-of-sight velocity dispersion function (LOSVD) to the observed spectrum. The galaxy model is obtained through this parametrization (in pixel space x):

$$G_{\rm mod}(x) = \sum_{n=1}^{N} w_n \{[T_n(x) * f_n(cx)] \sum_{k=1}^{K} a_k \mathcal{P}_k(x)\} + \sum_{l=1}^{L} b_l \mathcal{P}_l(x) + \sum_{j=1}^{J} c_j S_j(x), \quad (1)$$

where the w_n are the spectral weights, the $\mathcal{P}_k$ and $\mathcal{P}_l$ are multiplicative and additive orthogonal polynomials, respectively, and S_j are the sky spectra. The polynomials and sky spectra are optional components of the parametrization. The LOSVD $f(cx) = f(v)$ is parametrized by a series of Gauss–Hermite polynomials as

$$f(v) = \frac{1}{\sigma\sqrt{2\pi}} \exp\left(\frac{1}{2}\frac{(v-V)^2}{\sigma^2}\right)\left[1 + \sum_{m=3}^{M} h_m H_m\left(\frac{v-V}{\sigma}\right)\right], \quad (2)$$

where V is the mean velocity along the line of sight, σ is the velocity dispersion, H_m are the Hermite polynomials, and h_m are their coefficients. The best-fitting template is then found by χ^2 minimization. To compute our synthetic galactic spectrum, we chose The Indo-US Library of Coudé Feed stellar spectra (Valdes et al. 2004), a library of 1273 stellar spectra covering a broad range of parameters (effective temperature, metallicity, surface gravity) with a wavelength range of 3460–9464 Å and a spectral resolution of 1.35 Å (FWHM), $\sigma \sim 30$ km s^{-1}, and $R \sim 4200$. We use the `ppxf` method convolving the library to our last spectrum, taken after the

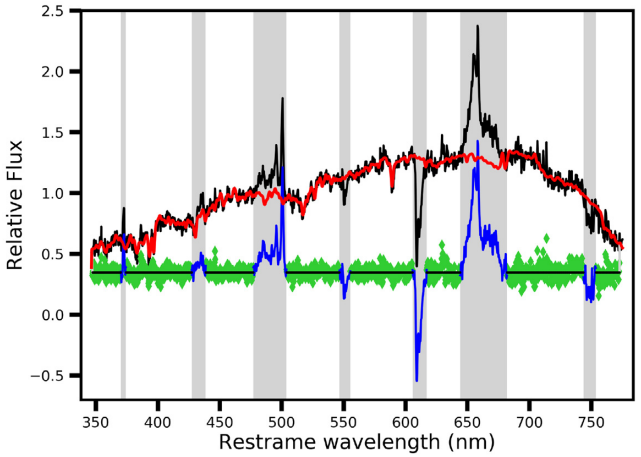

Figure 13. Fit of the stellar libraries to our last spectrum (2018 July 8, 894 d after peak) using the `ppxf` method. In black the observed spectrum, and in red, the best fit of the templates from the stellar library. The grey bands represent the areas excluded from the fit. In green and blue the subtracted spectrum is shown.

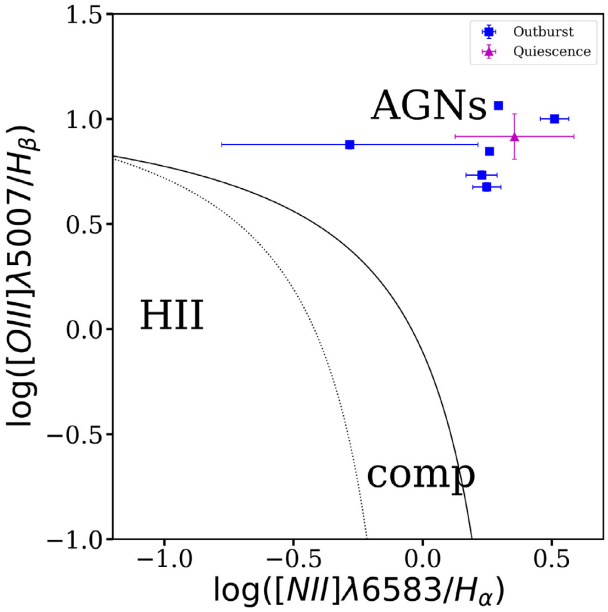

Figure 14. Plot of the position of the source on a Baldwin, Phillips, and Terlevich (BPT) diagram (Baldwin et al. 1981) using the narrow emission lines detected in the host spectrum of Gaia16aax, during the outburst (blue squares) and after it went back to the pre-outburst state (magenta triangle). In all cases, the position is consistent with the AGN region of the diagram. The lines that separate the different activity regions come from Kewley et al. (2001) (dotted line) and Kauffmann et al. (2003) (solid line).

object went back to its pre-outburst state. We excluded from the fit the regions in which the AGN lines are present, the regions of telluric absorption, and the edges of the spectrum. The template fit is shown in Fig. 13. We then subtract the galaxy spectrum obtained with this method from the spectra at all other epochs. The analysis presented from here onward is performed on the galaxy-subtracted spectra.

To analyse the complex emission-line structure, we fit the spectra with a combination of Gaussian function using a PYTHON code employing the LMFIT[12] package (Newville et al. 2014). The results of the line fits are listed in Table A2. During the outburst, except for the last two epochs, the H β emission-line complex can be well described by two Gaussian components: component A and a red wing, component B (H β_A and H β_B from here on); see Fig. A1. H β_A is blueshifted with respect to the rest-frame wavelength of H β (the shift is between ∼5 and ∼20 Å, corresponding to a velocity between ∼300 and ∼1000 km s^{-1}) while the red wing is redshifted with respect to the rest-frame wavelength by a factor that varies between ∼50 and ∼80 Å (corresponding to a velocity between ∼3000 and ∼5000 km s^{-1}). In the H β region, there are also two [O III] emission lines at their rest-frame wavelength (4959 and 5007 Å). The separation between the [O III] lines and their FWHM has been kept fixed during the fit.

The presence of the telluric absorption that falls on top of the H α region at the redshift of the object made a precise analysis of the H α region difficult. Overall, the H α emission-line complex displays a morphology similar to the one of H β (see Fig. A2): two components of which one (component A, H α_A from here on) is blueshifted with respect to the rest-frame wavelength (shift between ∼8 and ∼15 Å, corresponding to a velocity between ∼300 and ∼700 km s^{-1}) and a red wing (component B, H α_B from here on) that is shifted by around 100 Å (corresponding to a velocity of ∼4500 km s^{-1}).

In addition to these two components, we also fit the two [N II] lines (6550 and 6585 Å) and [S II] (6718 and 6733 Å, unresolved in our spectra). To reduce the numbers of free parameters in the fit of the H α region, we constrained the FWHM of the narrow lines to be the same as the value of [O III] in the fit to the H β region at the same epoch, under the assumption that the lines coming from the NLR do not change on the time-scale of the outburst we are analysing in this manuscript and the assumption that lines of different metals have the same FWHM. The separation between the two [N II] lines has also been kept fixed during the fitting procedure. On the spectrum of 2016 December 9 (MJD 57 732), a cosmic ray hits the detector exactly on the H β_A component; therefore, we did not display the results from the line fitting at this epoch for both H β components. During the time covered by our observations, the line parameters show variations above the statistical noise, without a clear evolution with time.

At the first two epochs (see Figs A2a and b), there is a narrow component (FWHM ∼ 170 km s^{-1}) on top of the red wing of H α, centred at ∼6650 Å. This component is not present in the subsequent spectra and we associate it with either He I 6678 Å or Fe I 6648 Å. Neither element is clearly present at other wavelengths, but He II 4686 Å, as well as other iron lines, could be present, but there is no clear detection as the contrast with the continuum is too low. In Fig. A2, the fits to the H α line in all epochs are shown. It is worth noting that the H α line retains the double-peaked nature until our last spectrum, taken after the *Gaia* light curve reached the pre-outburst level of emission, while the H β is well described by only one component in the last two epochs. This could be due to the lower SNR of these spectra and the lower contrast between the H β and the continuum, with respect to the H α line.

In Fig. 14, we show the position of the source in a Baldwin, Phillips, and Terlevich (BPT) diagram (Baldwin, Phillips & Terlevich 1981). For the calculation of the ratios of the fluxes, we introduced a narrow H α and H β component. To do this, we first fitted this additional component in the first spectrum (the one with

[12] https://lmfit.github.io/lmfit-py/

the highest SNR), constraining its FWHM to be the same of the other narrow lines at the same epoch. In the subsequent spectra, we kept the parameters of the narrow H α and H β component fixed, within uncertainties, under the assumption that the narrow lines do not change over the time-scale of our follow-up. We measured the ratios for the NOT spectra taken during the outburst decay and our last spectrum taken when the source was back in its pre-outburst state. At all epochs in which the narrow H α and H β components could be constrained, the position in the BPT diagram is consistent with the AGN area of the diagram, meaning that the NRL is dominated by AGN ionization.

3.3 Black hole mass estimate

We use the M–σ_* relation (Ferrarese & Ford 2005) to obtain an estimate of the BH mass of Gaia16aax, using the width of the Ca H+K lines to estimate the velocity dispersion of the galaxy. For this calculation, we use the second spectrum of our follow-up, as it is the one with the highest SNR, after the first classification spectrum, but less contaminated by the outburst light. After correcting for the instrumental broadening (16.2 Å for a 1.0 arcsec slit), we calculate $\sigma = 264 \pm 58$ km s^{-1}and a BH mass of $M_{\rm bh} = (6.4 \pm 3.7) \times 10^8$ M$_\odot$. The uncertainty on this measure is large, considering the modest SNR of the spectrum and the resolution of the instrument. The scatter in the M–σ_* relation, which is 0.34 dex (Ferrarese & Ford 2005), contributes to the uncertainty of this mass estimate. The resulting Eddington luminosity is $L_{\rm Edd} = (7.9 \pm 4.5) \times 10^{46}$ erg s^{-1}.

We are able to use the same method also for Gaia16ajq, where the Ca H+K lines are visible in the outburst spectrum. We obtain a BH mass of $M_{\rm bh} \sim 4.5 \times 10^8$ M$_\odot$. In the case of Gaia16aka, the Ca H+K lines are not visible; therefore, we use two single-epoch (SE) scaling relations between the continuum luminosity, the width of the H α (Greene, Peng & Ludwig 2010) or H β (Vestergaard & Peterson 2006) line, and the BH mass. To obtain the continuum luminosity of the AGN and the width of the line, we first subtract the galactic component from the spectrum of Gaia16aka, using the `ppxf` procedure described before. We then fit the subtracted spectrum with multiple Gaussian components. From the SE relation described in Greene et al. (2010), using the width of the H α line, we obtain a BH mass of $M_{\rm bh} \sim 2.4 \times 10^7$ M$_\odot$, while from the relation between the BH mass and the width of the H β line we obtain $M_{\rm bh} \sim 3.7 \times 10^7$ M$_\odot$. It is important to notice that these SE relations are intrinsically uncertain and may only yield an order of magnitude estimate (Vestergaard & Peterson 2006).

4 DISCUSSION

Before discussing in detail the possible interpretations of Gaia16aax, it is worth summarizing the main properties of the event: The transient is coincident with the nucleus of a galaxy that hosts a radio-quiet QSO (∼0.02 arcsec separation), with an inferred $M_{\rm bh}$ of $\sim 6 \times 10^8$ M$_\odot$. The source brightened in the optical by 1 mag over a time-scale of ∼350 d, reaching a peak absolute magnitude of $M_{\rm G} = -22.17$ and started a smooth decay with $t^{-0.161 \pm 0.004}$, going back to its pre-outburst level of emission over 2 yr. Flaring activity of this magnitude was detected both in the MIR (with a time lag of ∼140 d) and in the X-rays. The first spectra showed a strong blue continuum, while in the subsequent epochs the object became redder. In the first spectrum, a blend of lines between H γ and H β is present; this could be due to a blend of the He II and Bowen fluorescence emission lines. During the outburst, the Balmer lines underwent a dramatic change in their morphology, showing a clearly separated double-peaked profile. The narrow lines did not change over the period of our observations. In the first epochs of observations, the spectra showed a strong blue continuum that disappeared with time. The red wings of both the H α and H β lines are offset from their rest-frame wavelength by several thousand km s^{-1} and this shift does not vary significantly in time. The width of the lines and their equivalent widths do not show significant evolution with time. The SED cannot be satisfactorily fitted using a single blackbody, and a reasonable fit, although not perfect, is obtained using two blackbody components.

4.1 AGN variability

The enhanced emission and change of appearance of the emission lines could have been caused by variability in the accretion disc. While typical AGN variability is of tenths of magnitudes over time-scales of some years (van Velzen et al. 2011), more extreme cases of variability have been found. In Rumbaugh et al. (2018), a big sample (∼1000 objects) of extremely variable quasars (EVQs) has been studied, finding that Quasars that show extreme variability (i.e. a change of the optical magnitude >1 mag) all have a low Eddington ratio ($L/L_{\rm Edd}$<0.3). They argued that EVQs are not a separate class of objects, but rather a subset of quasars that are accreting at low rates. While individual events may originate from peculiar phenomena, the majority of EVQs are thought to be caused by accretion-related events. Gaia16aax throughout all its outburst maintains an Eddington ratio below 0.3, in line with the sample of EVQs presented in Rumbaugh et al. (2018). However, the rapid time-scale of Gaia16aax sets it apart from the majority of the objects in Rumbaugh et al. (2018) sample. In their sample, there are around 50 objects out of 977 that reach the maximum amplitude variability in a time ≤400 d.

4.1.1 *Time-scale and discs*

It is of interest to compare the time-scales found in Gaia16aax (i.e. a rise time-scale of hundreds of days and a decay time-scale of years) with the characteristic time-scales associated with different aspects of accretion discs in AGNs.

Lawrence (2018) has recently refocused attention on a long-standing problem (see also Antonucci 2018) that quasar variability is not compatible with standard accretion disc theory. The problems are succinctly summarized by Dexter & Begelman (2019). In agreement with Lawrence's conclusion that 'the optical output we see comes entirely from reprocessing of a central source', Kynoch et al. (2019) argue that the most favoured explanation of the observations is that the variability at all wavelengths can be accounted for by an intrinsic change in the luminosity of the central object (and the brightening observed in Gaia16aax in UV and X-rays seems to confirm this) – presumably the central regions of the black hole accretion disc. Assuming that this is so, then it appears that the most severe problem is the time-scale of the variability (see also Stern et al. 2018).

Such large amplitude variations in luminosity must be caused by variations in the accretion rate in the inner accretion disc (e.g. within $R < 10$–$20R_{\rm g}$, where $R_{\rm g} = GM/c^2$ is the gravitational radius). At such radii for the more luminous quasars, standard accretion disc theory (Shakura & Sunyaev 1973) finds that the discs are radiation pressure dominated. In that case, the standard viscous time-scale for radial inflow $t_\nu \approx R^2/\nu$, where ν is the effective kinematic viscosity,

can be written as (e.g. Pringle 1981)

$$t_\nu \approx (\Omega\alpha)^{-1}(H/R)^2, \tag{3}$$

where Ω is the local disc angular velocity, and H/R is the disc aspect ratio, or, equivalently, in this case (cf. Dexter & Begelman 2019)

$$t_\nu \approx 43 \left(\frac{\alpha}{0.3}\right)^{-1} \left(\frac{\kappa}{\kappa_{\rm T}}\right)^{-2} \left(\frac{M}{10^8\,{\rm M}_\odot}\right) \left(\frac{\dot{m}}{0.1}\right)^{-2} \left(\frac{R}{10R_{\rm g}}\right)^{7/2} {\rm d}. \tag{4}$$

Here α is the usual viscosity parameter, and we have adopted the observed value of $\alpha \approx 0.3$ for fully ionized discs (King, Pringle & Livio 2007; Martin et al. 2019), κ is the opacity, $\kappa_{\rm T}$ is the electron scattering opacity, M is the black hole mass, and $\dot{m} = 0.1\dot{M}c^2/L_{\rm Edd}$ is the dimensionless accretion rate, where $\dot{m} = 1$ gives a luminosity at the Eddington limit, $L_{\rm Edd}$, for an assumed radiative efficiency of $\epsilon = 0.1$.

Thus, we see that while the inflow time-scale can be as short as months at very small radii, the time-scale depends strongly on radius. For example, in order to account for changing-look behaviour in which the whole of the inner disc region (out to $R \approx 50$–$100R_{\rm g}$) needs to be removed and/or added, the time-scale required would be of some 30–370 yr, according to equation (4).

4.1.2 *Cause of the variability*

In addition to the time-scale problem with standard discs, there is a more fundamental problem, which is that the reason for such discs to be variable at all has not been identified. Most of the ideas on what might cause fluctuations in the disc mass flow centre on local variability within the disc. Kelly, Bechtold & Siemiginowska (2009) and Dexter & Agol (2011) propose ad hoc thermal fluctuations within the disc (see also Nowak & Wagoner 1995; Ruan et al. 2014). Ingram & Done (2011) propose ad hoc local fluctuations in the accretion rate, $\dot{M}$. More physically, fluctuations in local magnetic processes have been proposed by Poutanen & Fabian (1999) (flares in the corona), Hawley & Krolik (2001) (instabilities in the plunging region of the inner disc), Hogg & Reynolds (2016) (fluctuations caused by local dynamo processes), and Riols et al. (2016) (cyclic dynamo and wind activity). As pointed out by King et al. (2004), all these ideas have the same fundamental drawbacks: the time-scales for the fluctuations are too short (typically a few local dynamical time-scales), in that they are much less than the local inflow time-scale and so do not propagate far radially. Thus, being essentially localized, they all produce low-amplitude fluctuations.

4.1.3 *Large amplitude variability*

The problem of producing large amplitude fluctuations in the luminosity of the disc requires a large amplitude fluctuation at small radii (where most of the accretion energy is released) but on a time-scale much longer than the dynamical time-scales at those radii (typically hours to days). This problem has been addressed by King et al. (2004), though in a different context. King et al. drew on an earlier idea by Lyubarskii (1997), who pointed out that if some mechanism could be found for varying the accretion rate at large radius, *on the time-scale for inflow at that large radius*, then the resulting accretion rate fluctuation would be able to propagate to small radii, and so produce a large-amplitude luminosity fluctuation on that time-scale. This is the underlying basis of the ad hoc fluctuation analysis of Ingram & Done (2011) and Ingram & Done (2012).

King et al. (2004) proposed a physical model that was able to generate accretion rate fluctuations in the disc on time-scales much longer than the local dynamical time-scale. The basis of the proposal is that from time to time at least some of the angular momentum of disc material is removed by a magnetic wind (cf. Blandford & Payne 1982) and not just by disc viscosity. In order for such a wind to be effective at a given radius, it is necessary that there is a strong enough poloidal field component threading the disc at that radius. Lubow, Papaloizou & Pringle (1994a) demonstrated that such a field cannot be transported inwards by the accretion flow itself, because, for an effective magnetic Prandtl number of unity [likely for magnetohydrodynamic (MHD) turbulence], the field can move radially through the disc on a time-scale $t_{\rm B} \approx (H/R)t_\nu$, that is with a speed $v_{\rm B} \sim (R/H)v_{\rm R}$, where $v_{\rm R} \approx \nu/R$ is the usual viscous flow speed. Thus, it is more likely that such a field, if it exists, must be generated locally by local MHD processes involving an inverse cascade in order to produce a field with a spatial scale of $\sim R$ necessary for a wind, from the dynamo disc scale $\sim H$. That such a process can occur in discs has been suggested by Tout & Pringle (1996) and Uzdensky & Goodman (2008).

Lubow, Papaloizou & Pringle (1994b) pointed out that such a locally driven wind can in principle produce an inflow velocity that is faster than the usual viscous flow speed $v_{\rm R}$. They proposed that if the effect of the wind became locally strong enough that the wind-driven inflow speed exceeded $v_{\rm B}$, then the poloidal field responsible for the wind could be dragged inwards. In that case, they suggested that there is the possibility for a wind-driven avalanche, which could sweep the inner disc regions inwards. Cao & Spruit (2002) and Campbell (2009) concur with this conclusion. An example of how such an avalanche might operate is to be found in the numerical simulations by Lovelace, Romanova & Newman (1994).

From the point of view of time-scales, this mechanism (if and when it occurs) has the advantage that it occurs on a time-scale shorter than the usual viscous time-scale (equation 4) by a factor of H/R, that is, on a time-scale

$$t_{\rm B} \approx 6 \left(\frac{\alpha}{0.3}\right)^{-1} \left(\frac{\kappa}{\kappa_{\rm T}}\right)^{-1} \left(\frac{M}{10^8\,{\rm M}_\odot}\right) \left(\frac{\dot{m}}{0.1}\right)^{-1} \left(\frac{R}{10R_{\rm g}}\right)^{5/2} {\rm d}. \tag{5}$$

At a radius of $R \approx 50R_{\rm g}$, this corresponds to a time-scale of about a year [335 d].

What remain, of course, very uncertain are the time-scales on which such avalanche episodes might recur, and how these might depend on specific disc properties. King et al. (2004) proposed a specific (speculative and, of course, ad hoc) model, which has some physical basis. They propose the basic idea that each disc annulus of width $\sim H$ acts as an independent producer of vertical field B_z, which varies stochastically on the local dynamo time-scale $\sim$10–20 Ω^{-1}. They suggest, further, that occasionally enough ($\sim R/H$) neighbouring annuli have B_z aligned to produce a poloidal field with a length-scale of $\sim R$, and that when that happens angular momentum can be lost to a locally produced magnetically driven wind. They find that most of the time such processes give rise to frequent small-amplitude luminosity fluctuations, but they do give one example of one such large-scale fluctuation that began at a few hundred $R_{\rm g}$, which swept rapidly inwards, reducing the overall disc surface density by almost an order of magnitude.

4.2 Supernova

To comprehensively survey all other plausible scenarios, we also consider if the observed outburst could be explained by a supernova explosion in the nuclear region of the galaxy. A supernova explosion in the proximity of the nucleus (or superimposed spatially on our line of sight) would not explain the shape change of the Balmer lines. On top of this, the absolute magnitude of the peak of the outburst ($M_G \simeq -22$) is uncomfortably high to be caused by an SN and SNe are rarely seen emitting at X-ray wavelengths (Dwarkadas & Gruszko 2012) and would not explain the observed enhanced X-ray luminosity. Finally, even with efficient conversion of kinetic energy to radiation, the total radiated energy of Gaia16aax strains most reasonable supernova scenarios. None the less, it is worth noting that Kankare et al. (2017) discuss an SN origin for the nuclear transient PS1-10adi, which happened in the nucleus of a galaxy hosting an AGN and radiated a total energy of $\sim 2.3 \times 10^{52}$ erg.

4.3 Microlensing event

Microlensing events have been invoked to explain highly variable AGNs: in Graham et al. (2017), 9 of the 51 objects analysed are well described by a single-lens model and Lawrence et al. (2016) have proposed that microlensing provides a good description for many of the objects in their sample.

A microlensing event could in principle explain the intensity of the outburst, but it would not be possible to explain the change in shape of the Hydrogen lines and their time evolution via this phenomenon alone. On top of this, if a microlensing event would indeed be the cause of the enhanced emission, we would expect the light curve to be symmetric, while in our case the decay is much shallower than the rise to peak. The presence of a secondary bump at late times in the *Gaia* light curve also disfavours a microlensing event.

4.4 Variable dust absorption

For completeness, we also investigate whether the change of appearance in Gaia16aax could be due to variable absorption in our line of sight. In the case of Gaia16aax, it is easy to see why this is not a viable explanation: Using the method described in MacLeod et al. (2016) from the monochromatic luminosity of the QSO at 5100 Å, we can estimate the size of the BLR to be $R_{BLR} \sim 10$ light days [with $\lambda L_\lambda(5100\,\text{Å}) \simeq 1 \times 10^{43}$ erg s^{-1}, from the SDSS spectrum] or $\sim 2.6 \times 10^{16}$ cm ~ 0.01 pc. We need to draw this curtain in the line of sight on a time-scale of $\sim$100 d (the rise time of the outburst), which means that the cloud must travel at (10/100)c or $v \simeq 3 \times 10^4$ km s^{-1}. To obtain the required reddening of $A_v \simeq 1$ mag, we would need a column density of (assuming a standard dust-to-gas ratio) $N_H \simeq 2 \times 10^{21}$ cm^{-2}; assuming a spherical cloud, this would lead to a volume density of $n \simeq N_H/R_{BLR} \simeq 2.3 \times 10^4$ cm^{-3}. Such an object would correspond to a dense core within a molecular cloud (Blitz & Williams 1999). Assuming that the object is in virial equilibrium, it must have an internal dispersion velocity of $\sigma \simeq (GM_{cloud}R_{BLR}^{-1})^{1/2} \simeq (Gm_pN_HR_{BLR})^{1/2} \simeq 30$ km s^{-1}. The difficulty of this scenario would be to have this cloud move at the required speed of $\sim 0.1\,c$.

If the cloud was closer to the observer, the requirement on the speed would be less stringent. Assuming that the cloud is at a distance of $d = fD_L$, with $0 < f < 1$ and D_L the luminosity distance (1.26 Gpc), then the required size of the cloud is $R = fR_{BLR}$ and the required velocity is $v = 3f \times 10^4$ km s^{-1}. The column density N_H must be kept fixed because of the required reddening value; therefore, the volume density (assuming a spherical cloud) must increase accordingly: $n \simeq 2.3 f^{-1} \times 10^4$ cm^{-3}. To maintain the cloud internal virial support, we will have $\sigma \propto f^{1/2}$.

If we consider a cloud in the outskirts of an intervening galaxy with a velocity of $v \sim 100$ km s^{-1}, we would need $f = 3 \times 10^{-3}$ and a cloud of size $R = 7.8 \times 10^{13}$cm $\simeq 6$ au and a density of $n \simeq 8 \times 10^6$ cm^{-3}. Considering instead a cloud in the Local Group, we would need $f = 10^{-4}$ to have $d = 126$ kpc. Then we would have $v \simeq 3$ km s^{-1}and $n \simeq 2.3 \times 10^8$ cm^{-3}. If the cloud is instead inside the Milky Way, we would consider $f = 10^{-5}$, $d = 12.6$ kpc and $n \simeq 2.3 \times 10^9$ cm^{-3}. In all these cases, the requirements on the velocity and/or the volume density of the intervening clouds make this scenario improbable. The fact that the outburst was observed with similar amplitude in the NIR and X-rays also plays against an absorption scenario: We would expect some form of reprocessing of the radiation at different wavelengths. In addition to this, the source is undergoing an outburst rather than a dimming episode and it is the first time it has been observed in such a state. This would mean that we would need a cloud with the described properties constantly obscuring the central engine, until a 'hole' with the right density gradient would expose the source to us. On top of this, it is unclear how a variable absorption scenario would explain the appearance of the double peaks in the Hα and Hβ emission lines. The delay observed between the peak of the *Gaia* and *WISE* light curves also disfavours this variable absorption scenario. In fact, if we suppose that the enhanced emission comes from de-obscuration rather than an accretion-related event, we would not expect the IR emission to change similarly to the optical emission. This is because in this scenario, the IR emission would emerge, in an isotropic fashion, from the dust heated by the central engine. If the central emission is not varying, even if the obscuration in our line of sight is changing, we would expect the IR emission from the dust to remain unchanged.

4.5 TDE

TDEs typically show a fast rise to a peak luminosity of around 10^{44} erg s^{-1}, followed by a decay that follows $t^{-5/3}$. The decay time of our outburst is too long to fall into the canonical picture of TDEs, but there have been examples of long TDEs, the most extreme cases being a decade-long TDE candidate; see Lin et al. (2017) and a long-lived TDE in a merging galaxy pair Arp 299 (Mattila et al. 2018). TDEs are known to show broad (up to 10 000 km s^{-1}) Hydrogen and/or Helium lines. The absence of colour and blackbody temperature evolution of Gaia16aax, albeit on the limited time span of our photometric and SED coverage, is compatible with a TDE scenario (Arcavi et al. 2014).

The high mass inferred for the SMBH, though, complicates the TDE scenario. In fact, a sun-like star will be swallowed whole by the SMBH if its mass is above 10^8 M$_\odot$. To explain Gaia16aax as a TDE, the disrupted star must be more massive and/or the SMBH must be rapidly spinning (Hills 1978; see also the TDE candidate ASASSN-15lh, Leloudas et al. 2016). For a maximally spinning BH, the limit on the BH mass for a TDE to take place can increase by an order of magnitude (Kesden 2012). The high spin, on top of the high BH mass, introduces new arguments in favour of a TDE interpretation. Depending on the BH spin and if the to-be-destroyed star's orbit is prograde or retrograde, the radiation efficiency can vary by a factor of 10 (Bardeen, Press & Teukolsky 1972); therefore, the presence of a spinning BH could justify the high energy output of the event. On top of this, simulations performed by Guillochon & Ramirez-Ruiz (2015) found that for massive BHs ($\gtrsim 10^7$ M$_\odot$) the

strong general relativistic effects produce a rapid circularization of the debris giving rise to a prompt flare, explaining the fast rise to peak of Gaia16aax.

If the BH is maximally spinning, the inner disc temperature will be higher than in the case of a non-rotating BH. We tried to constrain the upper temperature of the hotter of the two blackbodies that describe the SED by fitting the combined UV and optical magnitudes (up to ∼5000 Å in Fig. 11). Since the temperature depends on the size of the innermost stable circular orbit (ISCO; which is smaller for spinning BHs than for non-spinning ones), by constraining the maximum temperature of the hotter blackbody, we could constrain the size of the ISCO. The observed data are not compatible with the tail of a hot ($\sim 10^7$ K) blackbody, as the emitting region associated with such a blackbody has a size of $\sim 10^5 r_g$, where r_g is the gravitational radius. Therefore, we cannot constrain the spin of the SMBH.

TDEs are usually found and studied in inactive galaxies, although one of the canonical TDEs ASASSN 14li occurred in a low-luminosity AGN (Prieto et al. 2016). The theoretical predictions and observational properties of TDEs in galaxies that harbour an AGN are less well constrained. In Chan et al. (2019), it is shown that a stream of debris from a disrupted star will impact the accretion disc and drain the accretion disc from the point of impact inwards on time-scales shorter than the inflow time from a Shakura & Sunyaev (1973) disc, with time-scales that depend on the orbital parameters of the disrupted star. The disc will then replenish itself on the (longer) inflow time-scale. These two different time-scales could explain the difference between the observed rise and decay times. This scenario could also help to explain the shape of the H α and H β emission lines and the secondary peaks we observe in the light-curve decay. Initially, the debris stream coming from the disrupted star slams into the accretion disc, starting the drainage of the disc material, resulting in the enhanced luminosity. Due to the impact, some of the material will splash out at an angle. If we consider this outflowing material as part of the source of the H α and H β emission lines (the other one being the BLR), the inclination of the outflow angle with respect to our line of sight would explain the double-peaked shape of the lines. If the initial debris stream is dense enough, the stream will pierce through the accretion disc, and slam into the disc again at a subsequent passage. This multiple encounters between the stream and the disc would help explain the presence of the two bumps in the light-curve decay at ∼300 and ∼600 d from peak.

It is worth noting that in the case of a TDE interacting with an AGN disc, the interaction between the disrupted material and the accretion disc – and thus the observed properties – will highly depend on the angle of incidence. One could argue that the discovery of Gaia16ajq and Gaia16aka could play against a TDE interpretation, given the almost identical light curves and spectra of the three objects. None the less, there are differences between the three objects that could reflect a diversity of encounters between the tidal debris and the accretion disc. Only Gaia16aax shows two components in the H α and H β emission lines, which in our picture are associated with splashing material after the encounter between the debris stream and the accretion disc. Moreover, the light curve of Gaia16aka decays smoothly, without secondary peaks, while Gaia16ajq shows a very strong bump ∼400 d after peak. As stated before, the bumps in the light curve are associated with eventual multiple interactions between the debris stream and the accretion disc.

If the three events are due to TDEs around a spinning SMBH, Fig. 6 requires the characteristic time-scales involved (e.g. mass return time and cooling time) as well as the total energy output to be very similar in each case. The SMBH masses in these sources vary by a factor of ∼10, implying cooling and mass return times that vary by a factor of ∼2–3 for similar stellar mass and pericentre (see Chan et al. 2019, for the relevant equations). For the light curves to lie on top of each other as in Fig. 6, we would need fine-tuning between the stellar mass and radius, the SMBH mass, and the pericentre distance of the encounter. It is also possible that the *Gaia* selection criteria mean that we are biased towards flares of this form. Implying that there could be a large number of flares due to TDEs in AGNs that are not being detected efficiently by the *Gaia* Alerts system (e.g. Kostrzewa-Rutkowska et al. 2018).

We also note that Chan et al. (2019) suggest that parabolic TDEs should cause a dip in the AGN X-ray flux as the corona is obscured by the tidal tail. In Gaia16aax, the X-ray emission increases by almost one order of magnitude with respect to the pre-outburst value. If the X-ray flux observed is associated with the TDE, it implies that the TDE may have occurred close to the plane of the AGN disc. The fact that the object is still bright in the UV and X-rays years after the peak is also in line with what is seen in other TDEs (e.g. Brown et al. 2017; Jonker et al. 2019).

It is interesting to consider also the case of the TDE Arp 299-B-AT1, where Mattila et al. (2018) observed a high total radiated energy above 1.5×10^{52} erg. The TDE happened in a nucleus hosting a known AGN and the transient showed a very significant, slowly evolving IR emission coming from the dust surrounding the AGN.

4.6 Tidal disruption of a neutron star in the accretion disc

Another possible scenario that could potentially explain the similarity between the flares observed in the three *Gaia* objects is that of a neutron star (NS) tidally disrupted by a stellar mass BH in the AGN accretion disc. The mass of the BH required for the tidal disruption depends on the NS equation of state and, to a large extent, on the BH spin (see Lattimer & Schramm 1976; Shibata & Taniguchi 2011). While the electromagnetic signal coming from the NS–BH merger would be too weak to be visible against the high luminosity of the AGN, part of the NS material would be outflowing at relativistic speeds and hit the hydrogen-rich accretion disc, creating the observed flare. In this scenario, the flare is not directly related to the SMBH – as in the case of an accretion event – therefore it can more naturally explain the similar bolometric luminosity of the three events. A tidal encounter between a NS and a stellar mass BH in the proximity of an AGN accretion disc could be relatively common. Considering a distribution of NS and BH around the SMBH, a fraction of these objects will either have orbits on the disc plane, or will have orbits that intersect the disc and that will evolve to the orbital plane during the disc lifetime. Different objects within the disc will suffer different dynamical friction and will encounter each other at low relative velocities, favouring the creation of binaries (McKernan et al. 2012; Stone, Metzger & Haiman 2017)

In Fig. 15, we show a simple calculation of the energy released in such a scenario. On the *Y*-axis we have the mass in the outflow (a fraction of the total NS mass) and on the *X*-axis the velocity of the outflow. The solid lines represent the kinetic energy ($1/2Mv^2$) of the outflowing material (with M its mass and v its velocity).

In this scenario, to reach an energy release of the order of 10^{52} erg, we would need a fraction of the NS material, around 10 per cent, to be traveling at ∼0.6c, taking into account relativistic boosting, which is relevant at the considered velocity, that would help reach

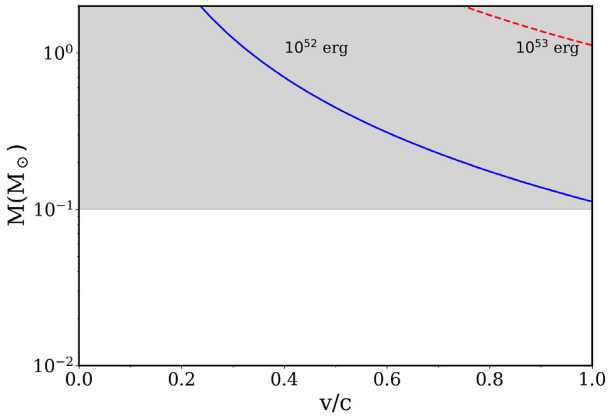

Figure 15. Energy ($1/2Mv^2$) release as curves for 10^{52} erg (blue solid curve) and 10^{53} erg (red dashed curve) plotted with mass of the ejecta on the *Y*-axis and its velocity on the *X*-axis. As shown in Barbieri et al. (2019), we do not expect more than 0.1 $M_\odot$ to be available for the NS ejecta; this limit is represented by the grey shaded area in the plot.

the required energy output. According to the calculations performed in Barbieri et al. (2019), 0.1 $M_\odot$ and 0.6*c* are the maximum values for the ejecta mass and velocity, respectively.

Gaia16aax released a total amount of energy of $\sim 3 \times 10^{52}$ erg; therefore, the energy provided by the dynamical ejecta is not enough to explain the emitted energy. Barbieri et al. (2019) suggest that a jet could also carry O(10^{52} erg) and in Deaton et al. (2013), a short-lived neutron-rich accretion disc around a rapidly spinning stellar mass black hole can have thermal energy also of O(10^{52} erg). Thus, we regard $\sim 3 \times 10^{52}$ erg as a reasonable upper limit for the energy output from a NS TDE, requiring a jet, fast and relatively massive and high-velocity ejecta and a rapidly spinning BH.

As said, the appeal of this picture lies in that it naturally explains the similar bolometric luminosity of the three events, something which is more difficult to do if it is related to accretion on to the central BH. The energy released during the Gaia16aax outburst (and, by extension, of the other *Gaia* objects), though, stretches this scenario, since its energy release is consistent with the upper limit calculated for this scenario. However, the total energy output of Gaia16aax could be underestimated, as our calculation of the bolometric luminosity was done mainly using the optical photometry from *Gaia*. If this is the case, the scenario discussed in this section must be ruled out.

5 SUMMARY

We present a multiwavelength follow-up of Gaia16aax, a nuclear transient discovered by the *Gaia* science alerts programme. The transient is coincident with a quasar at $z = 0.25$ (SDSS J143418.47+491236). The target brightened by more than 1 mag in the optical over less than 1 yr and went back to its pre-outburst level over more than 2 yr. Variability of similar amplitude has been detected also in the NIR (with a time delay of $\sim$140 d), UV, and X-rays. The most striking property of this object is the shape of the Hα and Hβ broad emission lines. These lines were present in the SDSS pre-outburst spectrum, but during the outburst they show two distinct peaks, at different shifts with respect to the rest-frame wavelength. Gaia16aax is part of a group of three nuclear transients discovered by the *Gaia* science alerts programme that showed nearly identical light curves. The other two are Gaia16aka and Gaia16ajq, for which a detailed follow-up is not available. The three objects show similarities also in their spectra.

We discuss various scenarios present in the literature to explain large-amplitude flares in AGNs to try to explain the observed properties of the outburst of Gaia16aax. The short time-scale of the rise to peak and the total energy output are the most challenging properties to explain. Of these scenarios, some are easily ruled out: a microlensing event, an SN explosion, and variable absorption in the line of sight cannot explain the observed properties. Other phenomena are more promising, although none can explain all the observed properties in a straightforward manner. The outburst of Gaia16aax can be explained by a change in the accretion flow on to the central BH. The low Eddington ratio of Gaia16aax is a characteristic shared by many other quasars that showed variability of similar amplitude. But, in the theoretical framework of accretion disc physics, it is difficult to explain the rapid rise shown by Gaia16aax, as the time-scales that govern the dynamics of an accretion disc are much longer than those at play in Gaia16aax. We review some proposed mechanisms in the literature for variability in the inner part of the accretion disc, finding that, with the aid of some magnetic wind-driven loss of angular momentum, a high amplitude variability on time-scales of $\sim$1 yr is possible, albeit the frequency of these episodes and their dependence on the disc properties remain uncertain.

The outburst could have been caused by a TDE. Given the high mass of the BH, to have a TDE the disrupted star needs to have a mass $\geq$1 $M_\odot$. The presence of star formation may allow for this. Certainly, for the stars of around a solar mass the BH must be rapidly spinning. This would help explain both the high energy release of the event and the short time-scale. The interaction between the debris stream and the accretion disc could help explain the shape of the light curve and the shape of the emission lines. The encounter between the debris stream and the accretion disc should give rise to different observable properties in the three *Gaia* objects, given the different SMBH masses and the dependence of such encounters on multiple parameters (e.g. density of the stream and incidence angle). The similar time-scale and peak brightness of the three transients question the validity of this scenario. We cannot exclude that the detection of the three similarly shaped flares is a product of the *Gaia* selection criteria and that we are missing more TDEs in AGNs. It is important to note that transient candidates detected by *Gaia* are vetted by eye before being published (Kostrzewa-Rutkowska et al. 2018) and it is therefore very difficult to gauge the selection function of *Gaia*.

We also explore the possibility that Gaia16aax is due to a NS–BH merger happening in the AGN disc. This scenario would help explain the three different transients independently of the central SMBH properties, but the high total energy output of Gaia16aax is on the high side of what is conceivably produced in this picture.

ACKNOWLEDGEMENTS

GC, PGJ, and ZKR acknowledge support from European Research Council Consolidator Grant 647208. MF is supported by a Royal Society – Science Foundation Ireland University Research Fellowship. FO acknowledges the support of the H2020 European Hemera programme, grant agreement no. 730970. JH acknowledges financial support from the Finnish Cultural Foundation and the Vilho, Yrjö and Kalle Väisälä Foundation (of the Finnish Academy of Science and Letters). BM and KESF are supported by National Science Foundation grant 1831412. CJN is supported by the Science and Technology Facilities Council (STFC) (grant number

ST/M005917/1). We thank the referee for their useful comments and suggestions. We acknowledge European Space Agency (ESA) *Gaia*, the Data Processing Analysis and Consortium (DPAC), and the Photometric Science Alerts Team (http://gsaweb.ast.cam.ac.uk/alerts). Based [in part] on observations made with the Nordic Optical Telescope (NOT), operated by the Nordic Optical Telescope Scientific Association (NOTSA) at the Observatorio del Roque de los Muchachos, La Palma, Spain, of the Instituto de Astrofisica de Canarias. The NOT Unbiased Transient Survey is supported in part by IDA (The Instrument Centre for Danish Astronomy). The data presented here were obtained [in part] with the Alhambra Faint Object Spectrograph and Camera (ALFOSC), which is provided by the Instituto de Astrofisica de Andalucia (IAA) under a joint agreement with the University of Copenhagen and NOTSA. The Liverpool Telescope is operated on the island of La Palma by Liverpool John Moores University in the Spanish Observatorio del Roque de los Muchachos of the Instituto de Astrofisica de Canarias with financial support from the UK (STFC). The Catalina Sky Survey is funded by the National Aeronautics and Space Administration (NASA) under Grant No. NNG05GF22G issued through the Science Mission Directorate Near-Earth Objects Observations Program. The Catalina Real Time Transient Survey is supported by the U.S. National Science Foundation under grants AST-0909182 and AST-1313422. Based on observations obtained with *XMM–Newton*, an European Space Agency (ESA) science mission with instruments and contributions directly funded by ESA Member States and NASA.

REFERENCES

Abolfathi B. et al., 2018, ApJS, 235, 42
Alard C., Lupton R. H., 1998, ApJ, 503, 325
Antonucci R., 1993, ARA&A, 31, 473
Antonucci R., 2018, Nat. Astron., 2, 504
Arcavi I. et al., 2014, ApJ, 793, 38
Baldwin J. A., Phillips M. M., Terlevich R., 1981, PASP, 93, 5
Barbieri C., Salafia O. S., Perego A., Colpi M., Ghirlanda G., 2020, EPJA, 56, 8
Bardeen J. M., Press W. H., Teukolsky S. A., 1972, ApJ, 178, 347
Becker A., 2015, HOTPANTS: High Order Transform of PSF ANd Template Subtraction, Astrophysics Source Code Library, record ascl:1504.004
Blagorodnova N. et al., 2019, ApJ, 873, 92
Blandford R. D., Payne D. G., 1982, MNRAS, 199, 883
Blitz L., Williams J. P., 1999, in Lada C. J., Kylafis N. D., eds, The Origin of Stars and Planetary Systems, NATO Science Series (Series C: Mathematical and Physical Sciences), Vol. 540, Springer, Dordrecht, NL
Blondin S., Tonry J. L., 2007, ApJ, 666, 1024
Bowen I. S., 1934, PASP, 46, 146
Bowen I. S., 1935, ApJ, 81, 1
Brightman M. et al., 2017, ApJ, 844, 10
Brown J. S., Holoien T. W. S., Auchettl K., Stanek K. Z., Kochanek C. S., Shappee B. J., Prieto J. L., Grupe D., 2017, MNRAS, 466, 4904
Campbell C. G., 2009, MNRAS, 392, 271
Cannizzo J. K., Lee H. M., Goodman J., 1990, ApJ, 351, 38
Cao X., Spruit H. C., 2002, A&A, 385, 289
Cappellari M., 2017, MNRAS, 466, 798
Cappellari M., Emsellem E., 2004, PASP, 116, 138
Chan C.-H., Piran T., Krolik J. H., Saban D., 2019, ApJ, 881, 113
Deaton M. B. et al., 2013, ApJ, 776, 47
Dexter J., Agol E., 2011, ApJ, 727, L24
Dexter J., Begelman M. C., 2019, MNRAS, 483, L17
Drake A. J. et al., 2009, ApJ, 696, 870
Dwarkadas V. V., Gruszko J., 2012, MNRAS, 419, 1515
Evans C. R., Kochanek C. S., 1989, ApJ, 346, L13
Evans P. A. et al., 2009, MNRAS, 397, 1177
Ferrarese L., Ford H., 2005, Space Sci. Rev., 116, 523
Gaia Collaboration, 2018, A&A, 616, A1
Gehrels N. et al., 2004, ApJ, 611, 1005
Graham M. J., Djorgovski S. G., Drake A. J., Stern D., Mahabal A. A., Glikman E., Larson S., Christensen E., 2017, MNRAS, 470, 4112
Greene J. E., Peng C. Y., Ludwig R. R., 2010, ApJ, 709, 937
Guillochon J., Ramirez-Ruiz E., 2015, ApJ, 809, 166
Hawley J. F., Krolik J. H., 2001, ApJ, 548, 348
Hills J. G., 1975, Nature, 254, 295
Hills J. G., 1978, MNRAS, 182, 517
Hodgkin S. T., Wyrzykowski L., Blagorodnova N., Koposov S., 2013, Phil. Trans. R. Soc. A, 371, 20120239
Hogg J. D., Reynolds C. S., 2016, ApJ, 826, 40
Ingram A., Done C., 2011, MNRAS, 415, 2323
Ingram A., Done C., 2012, MNRAS, 419, 2369
Jester S. et al., 2005, AJ, 130, 873
Jonker P. G., Stone N. C., Generozov A., van Velzen S., Metzger B., 2020, ApJ, 889, 166
Jordi C. et al., 2010, A&A, 523, A48
Kankare E. et al., 2017, Nat. Astron., 1, 865
Kauffmann G. et al., 2003, MNRAS, 346, 1055
Kelly B. C., Bechtold J., Siemiginowska A., 2009, ApJ, 698, 895
Kesden M., 2012, Phys. Rev. D, 85, 024037
Kewley L. J., Heisler C. A., Dopita M. A., Lumsden S., 2001, ApJS, 132, 37
King A. R., Pringle J. E., West R. G., Livio M., 2004, MNRAS, 348, 111
King A. R., Pringle J. E., Livio M., 2007, MNRAS, 376, 1740
Kostrzewa-Rutkowska Z. et al., 2018, MNRAS, 481, 307
Kynoch D., Ward M. J., Lawrence A., Bruce A. G., Landt H., MacLeod C. L., 2019, MNRAS, 485, 2573
LaMassa S. M. et al., 2015, ApJ, 800, 144
Lattimer J. M., Schramm D. N., 1976, ApJ, 210, 549
Lawrence A., 2018, Nat. Astron., 2, 102
Lawrence A. et al., 2016, MNRAS, 463, 296
Leloudas G. et al., 2016, Nat. Astron., 1, 0002
Leloudas G. et al., 2019, ApJ, 887, 218
Lin D. et al., 2017, Nat. Astron., 1, 0033
Lodato G., King A. R., Pringle J. E., 2009, MNRAS, 392, 332
Lovelace R. V. E., Romanova M. M., Newman W. I., 1994, ApJ, 437, 136
Lubow S. H., Papaloizou J. C. B., Pringle J. E., 1994a, MNRAS, 267, 235
Lubow S. H., Papaloizou J. C. B., Pringle J. E., 1994b, MNRAS, 268, 1010
Lyubarskii Y. E., 1997, MNRAS, 292, 679
McKernan B., Ford K. E. S., Lyra W., Perets H. B., 2012, MNRAS, 425, 460
MacLeod C. L. et al., 2010, ApJ, 721, 1014
MacLeod C. L. et al., 2012, ApJ, 753, 106
MacLeod C. L. et al., 2016, MNRAS, 457, 389
Mainzer A. et al., 2011, ApJ, 731, 53
Marconi A., Risaliti G., Gilli R., Hunt L. K., Maiolino R., Salvati M., 2004, MNRAS, 351, 169
Martin R. G., Nixon C. J., Pringle J. E., Livio M., 2019, New Astron., 70, 7
Matt G., Guainazzi M., Maiolino R., 2003, MNRAS, 342, 422
Mattila S., Harmanen J., Reynolds T., Fraser M., Hodgkin S., Blagorodnova N., Wyrzykowski L., Kankare E., 2016, Astron. Telegram, 8669, 1
Mattila S. et al., 2018, Science, 361, 482
Merloni A. et al., 2015, MNRAS, 452, 69
Netzer H., 2019, MNRAS, 488, 5185
Newville M., Stensitzki T., Allen D. B., Ingargiola A., 2014, LMFIT: Non-Linear Least-Square Minimization and Curve-Fitting for Python. available at: https://doi.org/10.5281/zenodo.11813
Nicholl M., 2018, Res. Notes AAS, 2, 230
Nowak M. A., Wagoner R. V., 1995, MNRAS, 274, 37
Onori F. et al., 2019, MNRAS, 489, 1463
Osterbrock D. E., 1981, ApJ, 249, 462
Planck Collaboration XIII, 2016, A&A, 594, A13
Poutanen J., Fabian A. C., 1999, MNRAS, 306, L31
Prieto J. L. et al., 2016, ApJ, 830, L32

Pringle J. E., 1981, ARA&A, 19, 137
Rees M. J., 1988, Nature, 333, 523
Riols A., Ogilvie G. I., Latter H., Ross J. P., 2016, MNRAS, 463, 3096
Ruan J. J., Anderson S. F., Plotkin R. M., Brand t W. N., Burnett T. H., Myers A. D., Schneider D. P., 2014, ApJ, 797, 19
Rumbaugh N. et al., 2018, ApJ, 854, 160
Schlafly E. F., Finkbeiner D. P., 2011, ApJ, 737, 103
Shakura N. I., Sunyaev R. A., 1973, A&A, 24, 337
Shibata M., Taniguchi K., 2011, Living Rev. Relativ., 14, 6
Skrutskie M. F. et al., 2006, AJ, 131, 1163
Stanishev V., 2007, Astron. Nachr., 328, 948
Stern D. et al., 2018, ApJ, 864, 27
Stone N. C., Metzger B. D., Haiman Z., 2017, MNRAS, 464, 946
Tody D., 1986, in Crawford D. L., ed., Proc. SPIE Conf. Ser. Vol. 627, Instrumentation in Astronomy VI. SPIE, Bellingham, p. 733
Tout C. A., Pringle J. E., 1996, MNRAS, 281, 219
Urry C. M., Padovani P., 1995, PASP, 107, 803
Uzdensky D. A., Goodman J., 2008, ApJ, 682, 608
Valdes F., Gupta R., Rose J. A., Singh H. P., Bell D. J., 2004, ApJS, 152, 251
van Velzen S. et al., 2011, ApJ, 741, 73
Vestergaard M., Peterson B. M., 2006, ApJ, 641, 689
Wright E. L. et al., 2010, AJ, 140, 1868

APPENDIX A: ADDITIONAL MATERIAL

Table A1. Magnitude values in the optical and NIR.

MJD (d) (1)	u (2)	B (3)	V (4)	g (5)	r (6)	i (7)	z (8)	y (9)	J (10)	H (11)	K_s (12)
51671.30 (13)	···	···	···	···	···	···	···	···	15.96 ± 0.09	15.47 ± 0.14	14.64 ± 0.10
52402.00 (14)	19.75 ± 0.04	···	···	19.47 ± 0.02	18.65 ± 0.02	18.13 ± 0.01	17.71 ± 0.02	···	···	···	···
56938.05 (15)	···	···	···	19.69 ± 0.02	18.88 ± 0.02	18.34 ± 0.05	17.99 ± 0.06	17.76 ± 0.05	···	···	···
57462.24	18.94 ± 0.09	18.95 ± 0.09	19.01 ± 0.06	19.17 ± 0.08	19.25 ± 0.06	18.97 ± 0.05	···	···	···	···	···
57476.24	19.12 ± 0.07	19.07 ± 0.06	19.05 ± 0.06	19.25 ± 0.07	19.30 ± 0.04	19.08 ± 0.04	18.70 ± 0.04	···	···	···	···
57491.01	19.01 ± 0.06	19.15 ± 0.06	19.18 ± 0.07	19.40 ± 0.08	19.35 ± 0.05	19.90 ± 0.04	19.23 ± 0.08	···	···	···	···
57505.03	19.21 ± 0.07	19.22 ± 0.07	19.31 ± 0.09	19.54 ± 0.08	19.42 ± 0.07	19.12 ± 0.07	18.91 ± 0.11	···	···	···	···
57509.04	···	···	···	···	···	···	···	···	17.92 ± 0.04	16.79 ± 0.12	15.69 ± 0.06
57530.02	···	···	···	···	···	···	···	···	17.81 ± 0.03	16.61 ± 0.08	15.63 ± 0.06
57551.01	···	···	···	···	···	···	···	···	17.85 ± 0.04	16.62 ± 0.12	15.45 ± 0.06
57560.91	19.53 ± 0.08	19.64 ± 0.06	19.74 ± 0.07	19.90 ± 0.10	19.84 ± 0.05	19.38 ± 0.05	19.33 ± 0.12	···	···	···	···
57588.95	19.32 ± 0.39	19.72 ± 0.12	19.99 ± 0.10	20.00 ± 0.30	20.05 ± 0.07	19.42 ± 0.10	19.87 ± 0.21	···	···	···	···
57611.95	···	···	···	···	···	···	···	···	17.97 ± 0.08	16.65 ± 0.23	15.35 ± 0.05
57738.25	···	···	···	···	···	···	···	···	18.09 ± 0.07	17.64 ± 0.15	16.15 ± 0.06
57791.27	···	···	···	···	···	···	···	···	···	17.47 ± 0.13	16.22 ± 0.08
57837.03	···	···	···	···	···	···	···	···	19.18 ± 0.12	17.91 ± 0.29	16.58 ± 0.11
57937.97	···	···	···	···	···	···	···	···	19.68 ± 0.14	18.18 ± 0.14	17.79 ± 0.12

Notes: (1) MJD date of observations; (2), (5), (6), (7), (8), and (9) apparent magnitudes with 1σ uncertainties in the optical bands u, g, r, i, z, and y, in the AB system; (3) and (4) apparent magnitudes with 1σ uncertainties in the optical bands B and V, in the Vega system; (10), (11), and (12) extinction-corrected apparent magnitudes with 1σ uncertainties in the near-infrared filters J, H, and K_s, in the Vega system. The first three lines are the archival magnitudes from 2MASS (13), SDSS (14), and PanSTARRS (15); all the other values are the result of the image subtraction procedure. The symbol ··· indicates an epoch in which an observation for the specific filter was not available.

Table A2. Results from the line fitting procedure on H α and H β.

MJD[(1)]	H β_A FWHM[(2)] (km s^{-1})	H β_B FWHM[(2)] (km s^{-1})	H β_A flux[(3)] (erg cm^{-2} s^{-1})	H β_B flux[(3)] (erg cm^{-2} s^{-1})	H β_A shift[(4)] (km s^{-1})	H β_B shift[(4)] (km s^{-1})	H α_A FWHM[(2)] (km s^{-1})	H α_B FWHM[(2)] (km s^{-1})	H α_A flux[(3)] (erg cm^{-2} s^{-1})	H α_B flux[(3)] (erg cm^{-2} s^{-1})	H α_A shift[(4)] (km s^{-1})	H α_B shift[(4)] (km s^{-1})
57428.27	3134 ± 206	4775 ± 466	197 ± 19	210 ± 22	-833 ± 104	3593 ± 201	4168 ± 152	4464 ± 541	850 ± 51	318 ± 46	-520 ± 114	4464 ± 299
57571.06	4340 ± 238	3724 ± 495	316 ± 20	96 ± 15	-394 ± 105	4492 ± 292	3778 ± 120	3856 ± 391	1180 ± 70	414 ± 47	-560 ± 88	4186 ± 169
57600.97	3801 ± 482	5914 ± 1696	112 ± 34	107 ± 35	-1064 ± 302	2905 ± 1157	3767 ± 178	3482 ± 493	526 ± 42	168 ± 26	-667 ± 117	4322 ± 191
57732.25	4590 ± 445	6192 ± 884	113 ± 15	93 ± 25	-795 ± 133	3514 ± 636	4069 ± 212	6400 ± 704	468 ± 47	338 ± 40	-537 ± 122	5265 ± 336
57780.26[(5)]	···	···	···	···	···	···	4410 ± 141	5294 ± 161	637 ± 34	342 ± 11	-671 ± 110	4766 ± 226
57845.15	4390 ± 281	5450 ± 1119	155 ± 13	77 ± 18	-655 ± 133	5403 ± 374	4050 ± 114	5301 ± 370	686 ± 51	383 ± 31	-936 ± 97	4371 ± 118
57935.94[(6)]	5008 ± 862	···	70 ± 18	···	68 ± 295	···	4145 ± 267	6234 ± 620	297 ± 32	295 ± 32	-1130 ± 114	4955 ± 221

Notes: (2) Full Width at Half-Maximum; (3) Equivalent Width; (4) shift of the central wavelength with respect to the laboratory wavelength of H α and H β. A negative value corresponds to a blueshift, and a positive value to a redshift. (5) In the spectrum taken on 2016 December 10, a cosmic ray hits the CCD at the location of the H β_A component; therefore, the results of the fit on the H β line are not reliable for this epoch. (6) At this epoch, the H β_B component is not present anymore. The last observation (MJD 58 307.01) was not analysed as the object was back to its 'quiescent', pre-outburst state at this epoch.

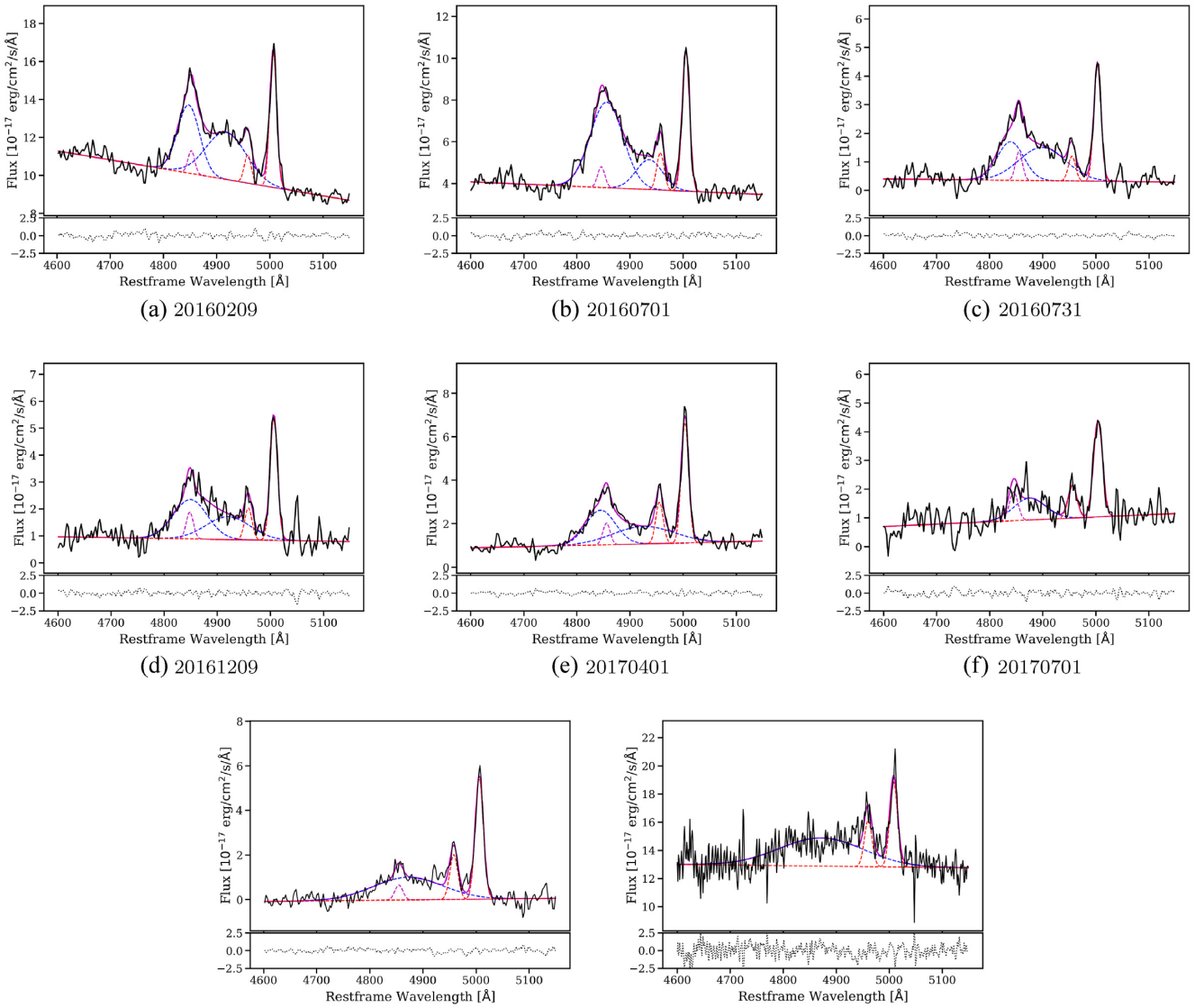

Figure A1. Evolution in time of the H β line region with the fit to the various components with multiple Gaussian curves. In all the panels, the blue dashed lines are the two H β components, the magenta dashed line is the narrow H β component, and the red dashed lines are the two [O III] emission lines. The spectra of 2017 January 26 are not shown since a cosmic ray hits the CCD on top of the H β line, making the results of the fit unreliable even after several attempts at correcting the data. Panel g is the H β line region at an epoch when the *Gaia* light curve has reached the pre-outburst level. The double-peaked shape of H β shown in outburst is not clearly present anymore at the last two epochs (panels f and g). The last panel is the SDSS spectrum, obtained well before the outburst start.

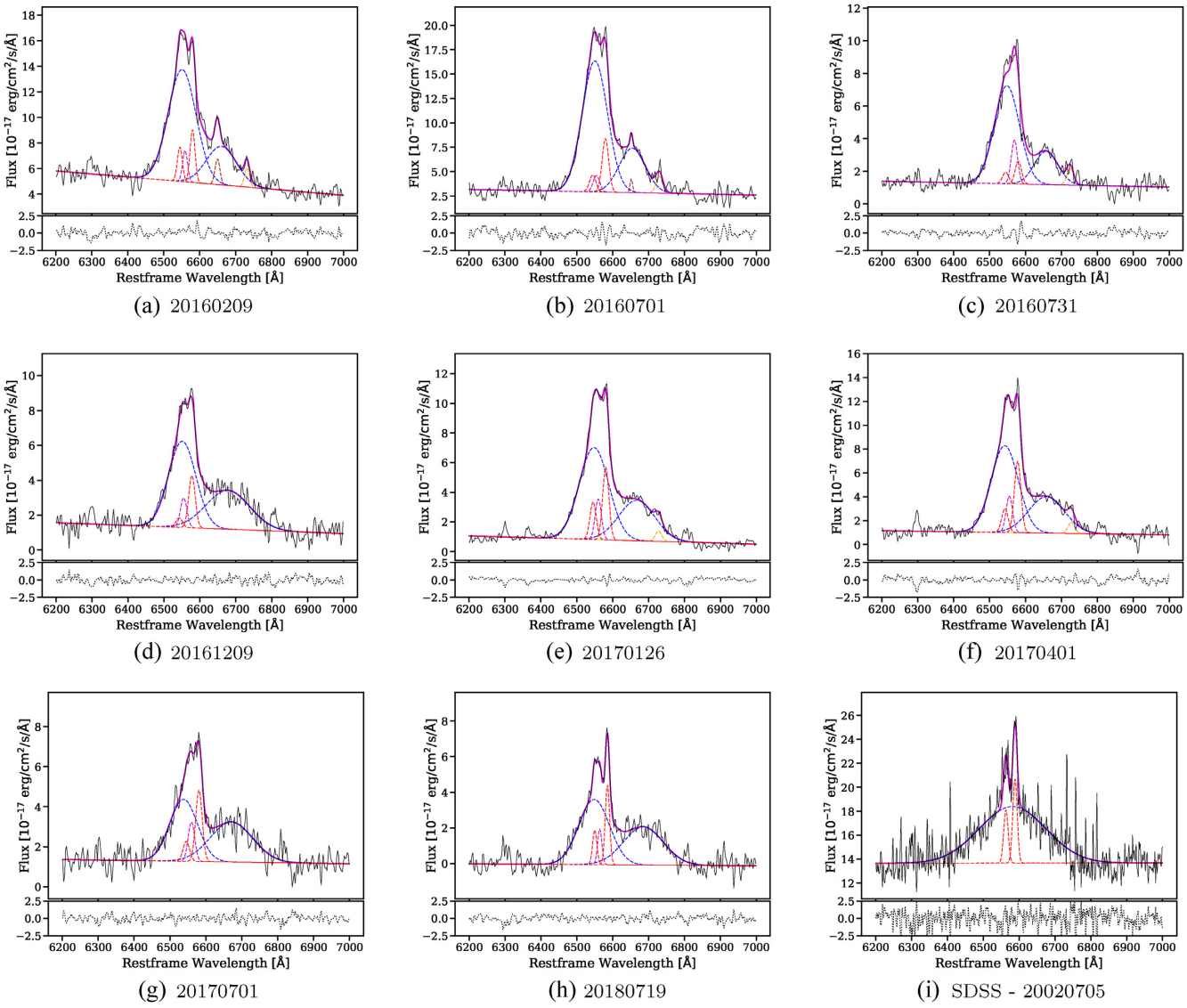

Figure A2. Evolution in time of the Hα line region with the fit to the various components with multiple Gaussian curves. In all the panels, the red dashed lines are the two [N II] lines, the blue dashed lines are the two Hα components, the magenta dashed line is the Hα narrow component, the brown dashed line is the He I line (only present in the first two panels a and b), and the orange dashed line is the blend of the two [S II] lines. Panel h is the spectrum taken after the object returned to its pre-outburst state, according to the *Gaia* light curve.

This paper has been typeset from a TEX/LATEX file prepared by the author.